

**CubeSat Altimeter Constellation Systems
Performance Analysis and Methodology**

Li, Yuanhao; Hoogeboom, Peter; Dekker, Paco Lopez; Mok, Sung Hoon; Guo, Jian; Buck, Christopher

DOI

[10.1109/TGRS.2021.3100850](https://doi.org/10.1109/TGRS.2021.3100850)

Publication date

2021

Document Version

Final published version

Published in

IEEE Transactions on Geoscience and Remote Sensing

Citation (APA)

Li, Y., Hoogeboom, P., Dekker, P. L., Mok, S. H., Guo, J., & Buck, C. (2021). CubeSat Altimeter Constellation Systems: Performance Analysis and Methodology. *IEEE Transactions on Geoscience and Remote Sensing*, 60. <https://doi.org/10.1109/TGRS.2021.3100850>

Important note

To cite this publication, please use the final published version (if applicable).
Please check the document version above.

Copyright

Other than for strictly personal use, it is not permitted to download, forward or distribute the text or part of it, without the consent of the author(s) and/or copyright holder(s), unless the work is under an open content license such as Creative Commons.

Takedown policy

Please contact us and provide details if you believe this document breaches copyrights.
We will remove access to the work immediately and investigate your claim.

CubeSat Altimeter Constellation Systems: Performance Analysis and Methodology

Yuanhao Li¹, Member, IEEE, Peter Hoogeboom, Paco López Dekker², Senior Member, IEEE, Sung-Hoon Mok, Jian Guo³, and Christopher Buck

Abstract—Multiple CubeSat altimeters can work independently or corporately to form altimeter constellations. Different configurations of the constellations can acquire distinguished advantages: improved spatial/temporal sampling and high cross-track resolution, which will be helpful for observations of oceanic small-scale structures and weather forecasting. Compared to single conventional altimeters, CubeSat altimeter constellations may achieve better performances with lower costs. To fully understand these systems, this article focuses on the performance analysis and methodology for CubeSat altimeter constellations. Besides the typical analyses of the resolution, revisit, and absolute sea surface height (SSH) accuracy, the performance analysis was conducted by considering the characteristics of multiple measurements provided by CubeSat altimeter constellations. Local and global spatial sampling performances are investigated for various constellations and compared by sampling density and swath size. Moreover, relative SSH accuracy is introduced and evaluated based on the spatial structure functions of errors to effectively evaluate the measurement performance. Related system requirements on power, delta-v, etc., to achieve the performance are also discussed, which ensures that the analysis fits the boundary conditions of implementation. Finally, different concepts of the CubeSat altimeter constellations are compared, where their limitations and possible solutions are also discussed.

Index Terms—Constellation, CubeSat, performance analysis, radar altimeter.

I. INTRODUCTION

SPACEBORNE radar altimeters can provide highly accurate measurements of sea surface height (SSH), significant wave height (SWH), inland water height, ice thickness, etc., by looking at the power and the shape of the return

Manuscript received February 14, 2021; revised May 31, 2021; accepted July 14, 2021. This work was supported in part by the European Space Agency (ESA) Research Fund under Contract 4000128550/19/NL/FE, in part by the Netherlands Organisation for Scientific Research (NWO) through the Dutch Knowledge Network on Radar Instruments and Applications (NL-RIA) Project, and in part by the National Natural Science Foundation of China under Grant 61960206009. (Corresponding author: Yuanhao Li.)

Yuanhao Li is with the School of Information and Electronics, Beijing Institute of Technology, Beijing 100081, China, and also with the Department of Geoscience and Remote Sensing, Delft University of Technology, 2628 Delft, The Netherlands (e-mail: lyh.900101@163.com).

Peter Hoogeboom and Paco López Dekker are with the Department of Geoscience and Remote Sensing, Delft University of Technology, 2628 Delft, The Netherlands.

Sung-Hoon Mok and Jian Guo are with the Faculty of Aerospace Engineering, Delft University of Technology, 2628 Delft, The Netherlands.

Christopher Buck is with the Radio Frequency (RF) Payload and Systems Division, European Space Research and Technology Centre, European Space Agency, 2201 Noordwijk, The Netherlands.

Digital Object Identifier 10.1109/TGRS.2021.3100850

pulses [1]. With the help of the launched altimeter missions (e.g., CryoSat-2, Sentinel-3, etc.), nowadays altimeter data can already resolve the observation scales of approximately 100-km wavelength for the ocean with an accuracy of a few centimeters in the best case [2], [3]. These continuous and reliable observations are very useful in obtaining the knowledge of ocean currents [4], annual sea level rise [5], and the kinetic energy changes of ocean circulation on a global scale [6], [7].

Besides sea-level changes and large-scale structures, researchers tend to be more interested in the observations of the small-scale structures in the ocean, such as a finer part of mesoscales (50–100 km) and even some sub-mesoscale features (kilometer-level) [8], [9], coastal regions, and extreme weather activities on the ocean. Small-scale features relate to energy dissipation, cascades, and interactions between different oceanic structures and layers and even connect to ocean topographies and submesoscale cyclones [10]–[12]. Observations at finer scales can help understand these energy transformation processes [13]. The observations in the coastal regions can support the research on seashore hydrodynamic variations with waves, upwelling, and nearshore interactions between currents and waves [7]. By data assimilations, these data can contribute to the validation of nearshore dynamic physical prediction models. Moreover, altimeter data can provide wind-speed information and improve the prediction accuracy of SWH from physical models, which is useful for safe transportation and other activities at sea under storms [14].

Since distinct applications relate to the oceanic targets with different temporal and spatial characteristics [15], they pose various requirements on radar altimeters, which are summarized in Fig. 1. To observe small-scale structures, a two-dimensional (2-D) spatial sampling density in the order of a few kilometers to dozens of kilometers is required according to the Nyquist sampling rule [16]. Meanwhile, compared to the measurement capability of current altimeter missions, a higher relative SSH measurement accuracy should be achieved because smaller-scale features generally have low amplitudes [17]. For nearshore observations, the system requires a sub-kilometer cross-track resolution to avoid the contamination from the nearby topography and the bright targets in very calm water patches within footprints [18]. In addition, a short-time revisit capability, e.g., an hourly revisit, is required to provide the weather forecasting for sea state when storms come. However, conventional altimeters

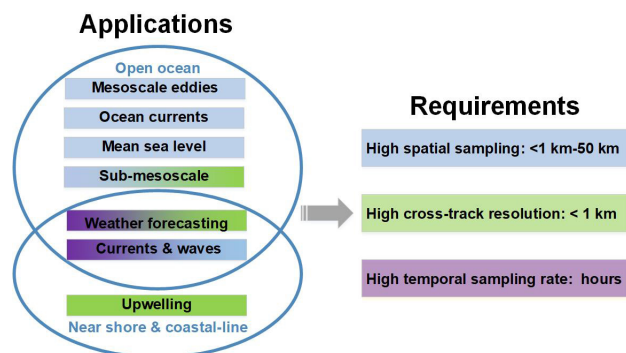


Fig. 1. Requirements on radar altimeter systems according to different observation applications.

cannot satisfy the aforementioned requirements. First of all, they can only improve the cross-track spatial sampling density by combining or interpolating the measurements from different tracks at different acquisition times, which is not useful for monitoring short-lifetime small-scale features [15]. For example, internal waves with 50-km scales only have lifetimes of several hours to about one day [15], [19]. Moreover, the SSH measurement accuracy in the current altimeters cannot distinguish the SSH variations between finer grids [20]. In view of geometric resolution, although the synthetic aperture radar (SAR) technique can be applied to improve along-track resolution, the best cross-track resolution is a few kilometers under the pulse-limited mode. At last, current spaceborne altimeters have a repeat cycle of several days to even more than one month, which cannot capture the evolution of extreme weather activities.

To address the above drawbacks, a wide swath altimeter, which is characterized by a high spatial resolution, is one option, such as the surface water ocean topography (SWOT) mission [21], [22]. Nevertheless, it is complex and expensive to be built because many advanced techniques need to be applied and a large platform is required. The other way is employing multiple altimeters [16], but the cost of traditional altimeters will inhibit the realization of such a constellation. Fortunately, with the development of CubeSat platforms, the goal can be achievable by using CubeSats instead. Due to their small sizes, CubeSat platforms can easily support a constellation mission which previously was not affordable with traditional large-satellites. The Satellite with ARGOS and ALtika (SARAL) can be in fact regarded as the first step toward future CubeSat altimeter missions [23]. An altimeter then can be implemented on a cheap and quick-turnaround CubeSat like the Raincube which is only 6U [24], and finally many of them can form a constellation. Based on the classical constellation configurations, some concepts of CubeSat altimeter constellations were presented, such as the bistatic and the quick-revisit formations [25], [26]. However, the detailed performance analysis and methodology for different CubeSat altimeter constellations are still missing. Without it, it is hard to fully understand the capability and the prospect of these CubeSat altimeter constellations, as well as the key techniques to build them.

In this article, we present the performance analysis and methodology for CubeSat altimeter constellation systems. First, aiming at distinguished spatial and temporal observation requirements, the typical configurations of CubeSat altimeter constellation missions are presented in Section II. These constellations are formed by multiple independent/cooperated CubeSat altimeters, which are characterized by any one advantage among a high spatial sampling density, a high cross-track resolution, and a high temporal sampling rate. In Section III, besides the traditional performance analysis in terms of revisit, resolution, and absolute SSH accuracy, local/global spatial sampling properties, swath sizes, and relative SSH accuracy are introduced to effectively reflect the capability and advantages of multiple measurements from the CubeSat altimeter constellations. We conduct elaborate analyses of these new indicators based on the formation geometries and the spatial structure functions of error sources which can be calculated from spatial error power spectra. It should be noted that we mainly focus on the analysis of measurement performance in oceanographic applications. Nevertheless, it can be extended to the measurement scenes in inland water and cryosphere since all these measurements are derived from the same waveform analyses. Taking the limitations of CubeSat platforms into account, the impact factors and optimizations of system performance have been discussed. Section IV provides the main system requirements on radio frequency (RF) power, antenna design, data rate, synchronization, formation control, and delta- v budget of different constellations. The technology readiness aspects for CubeSat altimeter systems and the system summary and comparison are discussed, respectively, in Sections V and VI. Finally, Section VII provides the conclusions of this article.

II. CUBESAT ALTIMETER CONSTELLATION CONFIGURATIONS

In this section, aiming at different oceanic applications with varied resolution and spatial-temporal observation requirements, we present the corresponding optimized configurations of CubeSat altimeter constellations. It should be noted that the following concepts can be combined to simultaneously improve all aspects of the observation.

A. Swath-Observing Altimeter Constellation

Swath-observing altimeter constellations aim at small-scale structure observation in the ocean. They can achieve instantaneous 2-D high spatial sampling within the short lifetimes of these small-scale features from their swath-observing capability. To achieve it, we require short-baseline formations by multiple nadir-looking altimeters or interferometric formations with bistatic operating mode [25].

1) *Comb Constellation*: The comb constellation is the most direct formation to achieve an instantaneous wide swath with multiple samples by setting up many identical CubeSat altimeters in a comb-like formation, which is shown in Fig. 2(a). Each CubeSat altimeter works individually and obtains independent cross-track observations of the ocean surface, thereby

forming a wide swath. Both cross-track combs and along-track combs can be distinguished. For a cross-track comb, they fly with separations in the cross-track direction (so, slightly different orbital planes) and slight separations in the along-track direction to avoid possible collisions at the poles for polar orbits. Differently, all CubeSats in along-track combs are on the same orbital plane with only along-track offsets. As illustrated in Fig. 2(a), because of the rotation of the earth, the time lag between CubeSats corresponds to a longitudinal separation of their footprints, which relates to different cross-track samples. In this way, several CubeSats in the along-track comb can also form a swath. The advantage of the along-track comb configuration compared with the cross-track comb is its easier formation acquisition at the beginning because distributing the satellites in the along-track direction requires much less orbit control efforts in terms of propellant use if sufficient flight time is given [27]. However, due to the time lag, it is not an instantaneous measurement, and the constellation loses the observation capability for very fast wave-current interaction processes. For comb constellations, because all the CubeSats are identical and working independently, building and sustaining the whole system is relatively simple and the applied techniques are more mature as well.

2) *Specular Constellation*: Besides purely working in a monostatic mode the comb constellation can also be designed to work under a bistatic mode. In this concept, as shown in Fig. 2(b), only the CubeSat in the center transmits signals, while all CubeSats distributed in the cross-track direction receive the specular reflections from the ocean surface. Setting different distances between the CubeSats, each receiver corresponds to a different specular region and measures a different part of the ocean surface. In this concept most of the CubeSats are simple receive devices with data links. Meanwhile, it also provides more flexibility to select the active platform, which can even be an enhanced CubeSat platform or a full-scale microsat to support more onboard instruments.

3) *Interferometric Swath Constellation*: An interferometric swath constellation can deliver many SSH samples over a swath with much finer ground-range resolution [21], [25]. Then, disturbing topography and bright scatterers in the coastal regions can be better suppressed, making the system helpful for monitoring the nearshore regions and the sub-mesoscale features in the ocean with kilometer-level scales or even finer. A sketch of this constellation is shown in Fig. 2(c). The active CubeSat illuminates at nadir and two passive CubeSats separated in cross-track direction operate as an interferometric pair. Thus, compared to the above two constellations, an interferometric swath constellation poses higher requirements on the system. In fact, this configuration is an extension beyond the specular constellation. According to the interferometric principle, for each range bin, the phase difference between the two CubeSat channels determines the direction where the received signal comes from. Then, the range of this signal is used to determine the actual height of the reflecting point. The achieved swath of the interferometric constellation is determined by the footprint of the CubeSats. It is narrower than that in the comb constellation but comparable to the swath

size in a specular constellation, which will be compared in Section III.

B. Short-Revisit Altimeter Constellation

Although the previous concepts can achieve wide swath observations by acquiring more spatial samples, their revisit time is still limited due to their similar orbit parameters. A short-revisit constellation, e.g., for emergency observations, requires CubeSats distributed along one or more orbit planes with a much larger distance between them up to thousands of kilometers. We can shorten the repeat cycles by adding orbit planes and/or satellites. While daily repeat orbits can be achieved with satellites on the single orbit plane [28], hourly repeat orbits require at least two orbit planes [29]. In this concept, like the comb constellation, the system is easy to build due to the identical and independently working platforms.

III. SYSTEM PERFORMANCE ANALYSIS AND OPTIMIZATION

In this section, we discuss the performance and its optimization of different constellations with respect to the swath width, the sampling density, the revisit performance, the sensor resolution, and the SSH accuracy. The constellation and system parameters that are used in the performance analysis are listed in Table I. These values stem from the preliminary design for CubeSat altimeters with some consideration and optimization in coverage, platform accommodation, and the baseline performance of the mission [25], [30].

A. Swath Size

Swath-observing altimeter constellations can provide simultaneous swath measurements rather than only a single-point measurement. The swath size in the comb constellation depends on the number of CubeSats and the distances between them. For a uniformly distributed formation, the swath length can be written as

$$l = (N - 1)d_c + \frac{\lambda}{D}h \quad (1)$$

where N is the number of CubeSats in the constellation, d_c is the distance between the CubeSats, h is the height of the CubeSat, λ is the wavelength of the carrier, and D is the length of the antenna. The first term in (1) expresses the gain in swath width due to the constellation. Increasing the swath width will raise the cost of the system. It should also be noted that the swath changes at different latitudes because the distance between the CubeSats changes along the orbit.

The observation swath is constrained by the half-power beamwidth of the transmit beam in the specular and interferometric swath constellations. Since an overlapped specular region in the footprint is required for enough echo power in the specular constellation, assuming the antenna sizes of the active and passive CubeSats are the same and their corresponding footprints are much larger than the pulse-limited resolutions,

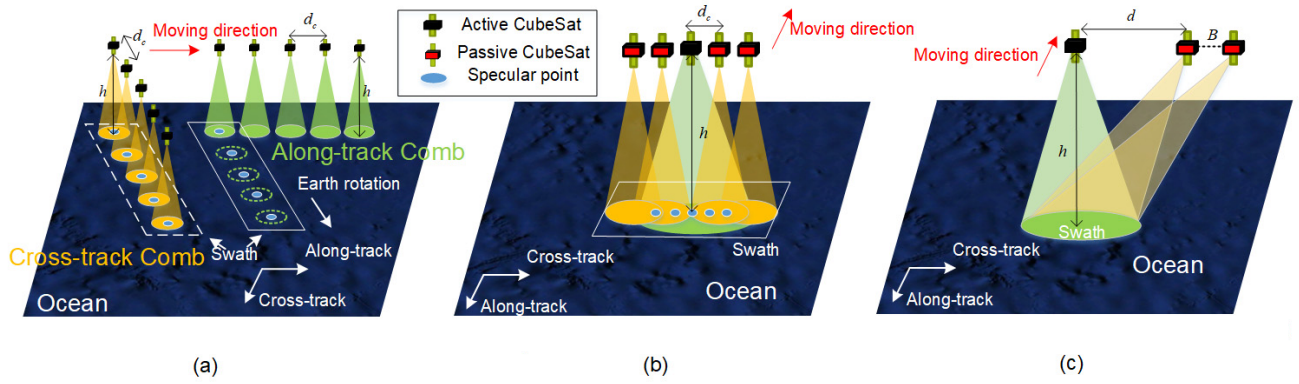


Fig. 2. Swath-observing altimeter constellations. (a) Comb constellation. (b) Specular constellation. (c) Interferometric swath constellation. h is the height of the CubeSats, d_c and d are the distances between the active CubeSat, and the passive CubeSat in the specular constellation (uniformly distributed) and the interferometric swath constellation, respectively, and B is the baseline between the interferometric pair.

TABLE I
CONSTELLATION AND SYSTEM PARAMETERS

Parameter	Value	Parameter	Value
Orbit type	Sunsynchronous	Orbit height (km)	634
Repeat cycle (days)	30	Number of orbits in one repeat cycle	443
Number of satellites	$5^{*1,2}/3^{*3}/20^{*4}$	Number of orbit planes	2^{*4}
Distance between CubeSats at the equator (km)	$50^{*1}/4^{*2}/24.1^{*5} \cdot 0.3^{*6}$	Inter-CubeSat phasing difference (deg)	108
Band	Ka	Cross-track antenna size (m)	0.8 (Monostatic) 0.5 (Bistatic)
Bandwidth (MHz)	500	Coherent pulses number per burst	10
Signal-to-noise ratio (SNR) (dB)	11	Pulse repetition frequency (PRF) (Hz)	4000 (Traditional) 18700 (SAR)
Burst repetition interval (ms)	4	Uncompressed pulse width (us)	48
Sigma0 (dB)	11^{*7}	Compressed pulse width (m)	0.3
Noise factor (dB)	5^{*8}	System temperature (K)	293
Lifetime (year)	1.5	Dry mass (kg)	11
Cross sectional area (m^2)	0.16	Drag coefficient	2.2

*1 Comb constellation; *2 specular constellation; *3 interferometric swath constellation; *4 short-revisit constellation; *5 and *6 the distance between the active CubeSat and the nearest passive one and the distance between the passive ones in the interferometric swath constellation; *7 the selected sigma0 is 1.5 dB under the lowest value calculated with the OceanSAR simulator for a wind speed ranging from 0 to 25m/s for a Ka-band radar altimeter. The simulator is available at <https://github.com/pakodekker/oceansar.git>; *8 These values are taken from our previous studies and validation based on the analyses for the CryoSat-2 and the SARAL [26].

a maximum swath size can be defined by

$$l = \begin{cases} \frac{3\lambda}{D}h - 2\rho_{cp}, & \text{pulse - limited mode} \\ \frac{2\lambda}{D}h, & \text{beam - limited mode} \end{cases} \quad (2)$$

where

$$\rho_{cp} = 2\sqrt{2hp} \quad (3)$$

is the pulse-limited resolution and p is the compressed pulsewidth. Under the pulse-limited mode, at least an overlapped area which is comparable to the pulse-limited resolution is required [31]; for the beam-limited case, the area is defined by at least 50% of the footprint.

For the interferometric constellation, because of its off-nadir observation geometry, its swath size is the entire footprint size, which is given by

$$l = \frac{\lambda}{D}h. \quad (4)$$

It can be seen that the swath size is independent of satellite number and distance between Cubesats in these cases. Albeit

the specular and the interferometric swath constellations will enable the detection of very small features, but only in a very small swath. The detection of larger features is not possible with these constellations, unless multiple of these constellations are used to form a comb constellation. The achieved swath sizes of different CubeSat altimeter constellations according to the parameters in Table I are listed in Table II.

B. Spatial Sampling Density

Spatial sampling density enables to compare the observation capability of these constellations for small-scale features. Most important is the local observation capability, which follows from a single instantaneous wide swath observation by the constellation. However, based on the orbit properties a global observation capability can also be distinguished, consisting of combined observations from multiple passes, hence nonsimultaneous and therefore only capable of observing features with sufficiently long lifetimes. In the analysis, we assume that the CubeSats are uniformly distributed in the constellations.

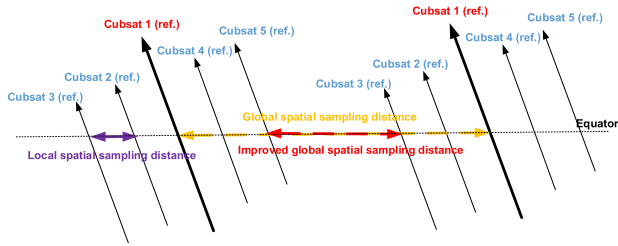


Fig. 3. Global and local spatial sampling definitions.

1) *Local Sampling Density*: The most important advantage of the swath-observing altimeter constellations is the achieved fine observation capability from their high local sampling densities in the swath. We can set up the distance between the CubeSats in the comb and specular constellations to observe the ocean features with desired scales. According to the Nyquist sampling rule, the distance should satisfy

$$d_c < \frac{x_0}{2} \quad (5)$$

where x_0 is the lower-bound of observation scales of oceanic structures. It should be noted that x_0 is assumed larger than the cross-track resolution of a single altimeter ρ_c . It is useless to try to measure small-scale phenomena with a spatial sampling rate that is smaller than the sensor's cross-track resolution. Meanwhile, the distance should also be larger than the required safety distance between the Cubesats d_s . Therefore, the lower-bound of the distance is given by

$$d_{c,low} = \max\left\{d_s, \frac{\rho_c}{2}\right\}. \quad (6)$$

In addition, since the orbits are separated the most at the equator and converge at the polars, in the cross-track comb and the specular constellations, (5) should be satisfied for the minimal d_c at the equator. Similarly, the required time lag in the along-track comb should be computed from the Earth rotation velocity at the equator and the projection angle between the cross-track direction and the longitude direction. In the interferometric swath constellation, its local sampling density relates to its range sampling rate.

2) *Global Spatial Density*: The global sampling distance for a single satellite is usually determined by the largest gap between measurements at the equator after the integration of the tracks by a period of time, which is shown as the orange dashed line in Fig. 3. The sampling distance is inversely proportional to the repeat cycle: a short distance can be achieved by sacrificing revisit time. Swath-observing altimeter constellations not only provide local sampling, they can also shorten the global sampling distance by their wide swaths. The red dashed line in Fig. 3 shows the decrease in gaps.

The gap after one repeat cycle is expressed by

$$d_g \approx \frac{2\pi R_e}{n_r} - l \quad (7)$$

where R_e is the equivalent radius of the Earth and n_r is the number of tracks in one repeat cycle of a single CubeSat.

In the comb constellation, the gap decreases with the increase of the intersatellite distance and the number of the

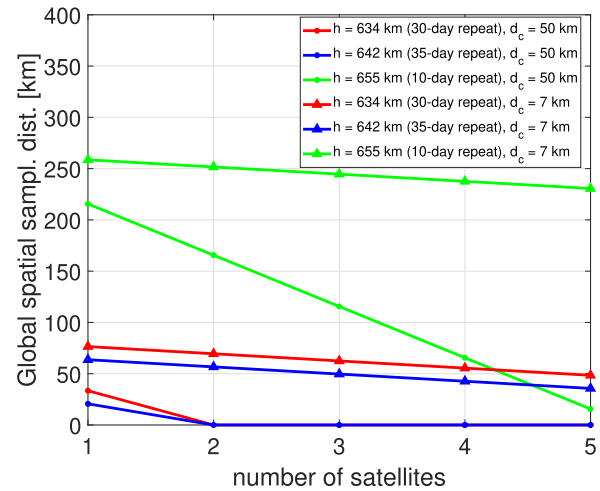


Fig. 4. Maximal gap between two measurements at the equator as a function of the number of CubeSats for different orbit heights, repeat cycles, and intersatellite distances at the equator in a comb constellation.

CubeSats. For example, Fig. 4 shows how the largest gap at the equator decreases when we put more CubeSats in the comb constellation. It illustrates that a larger intersatellite distance and a longer repeat cycle can help to improve global spatial sampling density. The maximum gap is zero for a 634-km altitude system with two satellites, in which case a complete global observation is realized. For the specular constellation, when the maximum swath size is obtained, the gap will no longer depend on the number of CubeSats and their distances, because the cross-track extension of the constellation is always small and limited by the antenna footprint dimensions.

Next, a simulation experiment was carried out to visually compare the performance of the cross-track comb and the specular constellation with a traditional single satellite altimeter. Fig. 5 shows the results in three columns. Left are the reference SSH anomaly data and the sampled tracks of different systems in a large area with two analysis boxes A and B indicated. The middle column has the results for box A (890 km × 280 km) and the right column for box B (4450 km × 2500-3300 km). This set with large-scale features (i.e., ≥ 50 km at the equator) is obtained from the SSH anomaly dataset of the Copernicus Climate Change Service (C3S) on 1st January 2019. Due to the resolution limitation of the C3S dataset, for finer SSH variations, we need to simulate them separately and added them into the dataset. The kinetic energy at the different scales follows a power-law spectrum with an index of -2 in the spatial wavenumber domain [32]. Therefore, we generate the random small-scale SSH variation (i.e., between 2 and 50 km) spatially with this spectrum and a standard deviation of 5 cm. Finally, the reference SSH data is the combination of both the C3S SSH data and the simulated small-scale SSH variation. The sampled tracks in the center and right columns are the observations of three days and we assume that the features in the ocean are stable during the observation time. The spatial sampling density in the along-track direction is about 7.5 km. Comparing these results, it can be seen that the comb constellation performs better in

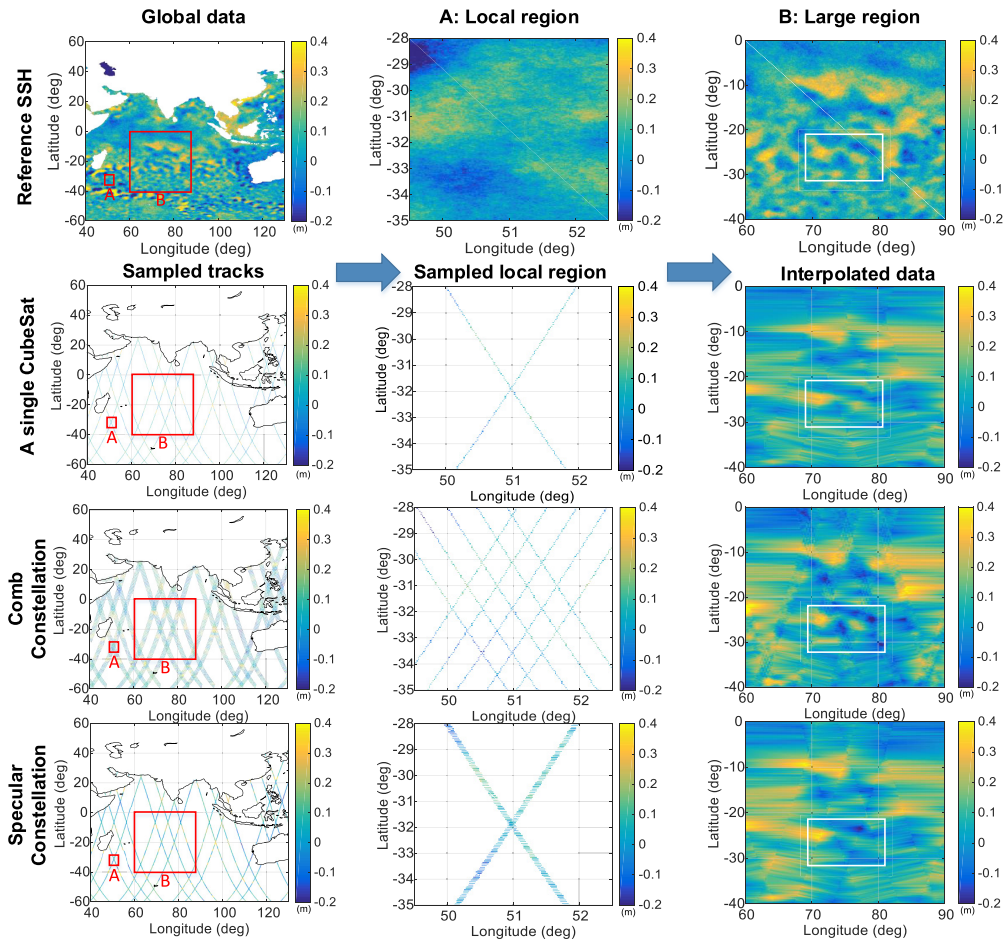


Fig. 5. Spatial sampling performance of different constellation configurations. The reference SSH anomaly data is simulated by two parts: the large-scale component and the small-scale variation. The large-scale component derives from the SSH anomaly dataset of the C3S on 1st January 2019. The small-scale variation is simulated by the random process with a power-law spectrum. The sampled tracks are the observations of three days and the spatial sampling density in the along-track direction is about 7.5 km. Both two constellations have five CubeSats. The distance between the CubeSats at the equator in the comb constellation is 50 km, and the distance in the specular constellation is 4 km.

the large area B than the single satellite and the specular constellation, which derives from its good global sampling performance from its largely separated multiple samples. In the small area A, the specular constellation performs better than the other two, because of the much improved local spatial sampling density. The spatial sampling performances in the studied case have been summarized in Table II.

Fig. 6 depicts the spatial-temporal measurement capability toward different ocean features by different altimeter systems. The conventional altimeters only work in the blue regions. Owing to simultaneously multiple measurements, comb, and specular constellations have their observation capabilities in the pink region, which suggests that they can break the spatial-temporal limitations of the conventional altimeters for the observation of oceanic small-scale features. For finer structures in the ocean (hundred meters to a few kilometers), we prefer an interferometric swath constellation rather than only a high spatial sampling density. In a view of spatial sampling performance, note that the specular constellation in fact can be regarded as a constricted version of the comb constellation in terms of the distances between the CubeSats.

It should be noted that we focus on the swath spatial sampling density of the constellations in the analysis, since their along-track sampling density depends on the posting rate like the conventional altimeters. Nevertheless, CubeSat altimeter constellations have advantages to overcome the issues of SAR altimeters in the observation of small-scale features in the along-track direction [33]. A quick-revisit capability in a short-revisit constellation can be converted to the benefit of local spatial sampling density in the along-track direction. Like the concept of along-track comb constellations, if the nearby satellites in a short revisit constellation (slightly different orbit planes) have a relative ground track repeat period of 6.7 s, the corresponding simultaneous along-track local spatial sampling density of the CubeSats is 50 km. In this way, the relative measurements in the constellation can reduce the errors from long ocean waves. In addition, a relatively large footprint can decrease the sensitivity of the system toward the swell effects.

C. Revisit Time

The revisit time can be defined here as the time between two consecutive observations of the same ground target, which

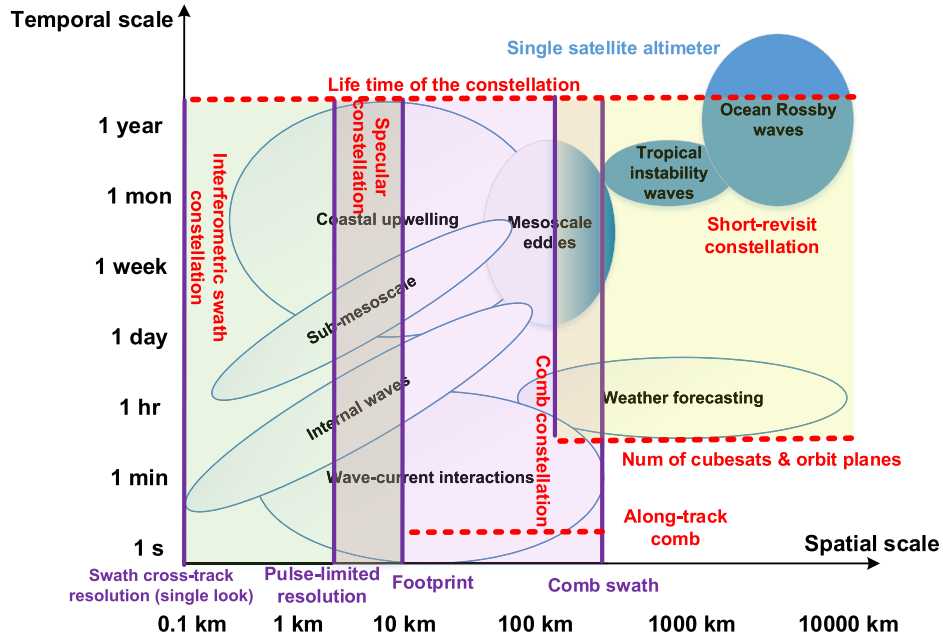


Fig. 6. Space and time scales of ocean features and the measurement capability of different altimeter systems. The blue filled items represent the observation scope of conventional altimeters [15]. The pink region is observation scope of the comb and specular altimeter constellations. Interferometric swath constellations work in the green region and the yellow region is covered by the short-revisit constellation.

TABLE II

PERFORMANCE OF THE SWATH SIZE, THE SPATIAL AND TEMPORAL SAMPLING, AND THE RESOLUTION FOR DIFFERENT CUBE-SAT CONSTELLATIONS

Property		Constellation			Short-revisit
		Swath-observing altimeter			
		Comb	Specular	Interferometric swath	
Swath size (km)		$\sim 207^{*1}$	~ 29 (pulse-limited) ~ 21 (beam-limited)	~ 11	-
Spatial sampling density	Global sampling gap ^{*1} (km)	No gap	~ 60 (pulse-limited) ~ 70 (beam-limited)	80	90
	Local sampling density ^{*1} (km)	50	~ 5	$\sim 0.01^{*3}$ (single-look)	-
Revisit	General revisit (day)	30		30	3
	Quick-revisit interval (hour)	-		-	3
Resolution	Cross-track (km)	6.7 (beam-limited) 1.2 (pulse-limited)		$\sim 0.01^{*3}$ (single-look)	6.7 (beam-limited) 1.2 (pulse-limited)
	Along-track (km)	6.7 (beam-limited) 1.2 (pulse-limited) $\sim 0.66^{*2}$ (SAR)		0.0005 (1 m along-track antenna)	6.7 (beam-limited) 1.2 (pulse-limited) $\sim 0.66^{*2}$ (SAR)

^{*1} at the equator; ^{*2} 10 coherent burst pulses; ^{*3} 2° mean incidence angle.

depends on the orbit, the target location, and the payload capability (i.e., resolution or swath width) for a single satellite. For a fixed orbit plane, the relative intersatellite phasing p_s between two satellites in the constellation to achieve a r_d days in repeat orbit is expressed by [34]

$$p_s = 2\pi r_d \frac{m-k}{m} \quad (8)$$

where m is the repeat-cycle of a single CubeSat and k is the prime integer to produce repetition fraction.

If a quick-revisit time of less than 24 h is required, we need to use more orbit planes, where the difference of the right ascension of the ascending node (RAAN) between the nearby two orbit planes ($\Delta\omega$) can be calculated by

$$\Delta\omega = 2\pi \frac{T_i}{T_E} \quad (9)$$

where T_i is the quick-revisit period and T_E is the sidereal day. Meanwhile, the required intersatellite phasing in mean anomaly between the nearby two orbit planes to make the repeated ground track can be obtained by [35]

$$p_{ms} = \text{mod}(-n\Delta T_i, 2\pi) \quad (10)$$

where n is mean orbital angular velocity.

Theoretically, if a revisit cycle of 3 h is required, we need 240 CubeSats uniformly distributed in eight orbit planes when a single CubeSat has a repeat cycle of 30 days. Special solutions requiring less CubeSats exist if we do not need uniform 3 h sampling throughout the repeat cycle, but, for instance, only two samples are needed with 3 h separation. In Fig. 7, we demonstrate one example of the short revisit constellations, where the corresponding revisit performance has been provided in Table II. We utilize two orbit planes

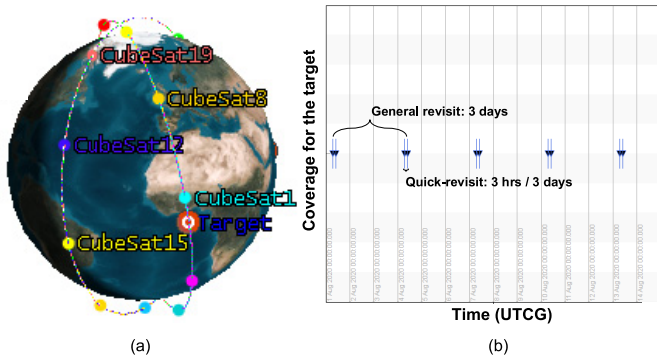


Fig. 7. Example of short-revisit constellation (a) and its revisit capability (b). All CubeSats are distributed in two orbit planes and each orbit plane has ten CubeSats. The simulation time period through the systems tool kit (STK) software in (b) is from 1st August 2020 to 14th August 2020 and the position of the observation target is at $(0^\circ, 0^\circ)$.

with a RAAN difference of 45° . In each plane, there are ten CubeSats uniformly distributed with an intersatellite phasing of 108° . Thus, the general revisit of the CubeSat constellation decreases from 30 to 3 days and we can achieve a quick-revisit of 3 h every three days. Following (8)–(10), we can distribute more CubeSats to improve both the general and short-revisit performances, while there is a trade-off with the cost of the constellation.

D. Resolution

The resolution of nadir-looking radar altimeters depends on the operating mode. In the beam-limited mode, the resolutions both in the cross-track and the along-track direction are limited by the footprint size. When implementing the pulse-limited mode, the resolution can be improved and depends on transmit bandwidth and orbit height [see (3)]. A lower orbit height and a wider transmit bandwidth can provide a better resolution. Thus, we prefer to implement pulse-limited mode for nadir-looking altimeters. In Table II, the pulse-limited resolutions in both the cross-track and along-track direction are worse than 1 km. If an unfocused SAR processing is exploited to achieve a higher ground resolution over a short aperture length, the along-track resolution improves and is expressed as [36]

$$\rho_a = \frac{\text{PRF} \cdot h \cdot \lambda}{2nv_s} \quad (11)$$

where v_s is the platform speed, PRF is the pulse repetition frequency, and n is the number of pulses for coherent processing in a single burst. If $n = 10$, the along-track resolution can be improved from more than 1 km to 600 m. More pulses can be used to further improve the along-track resolution with a maximum of half the along-track antenna length, while the resolution is also constricted by the surface decorrelation time [37].

The interferometric swath constellation can obtain not only a high along-track resolution by SAR processing but also a high cross-track resolution due to its off-nadir geometry and can distinguish the targets from different ground ranges. Its

cross-track resolution is expressed by

$$\rho_c = \frac{c}{2B_t \sin \theta_{\text{inc}}} \quad (12)$$

where c is the velocity of light, B_t is the signal bandwidth, and θ_{inc} is the incidence angle.

Increasing the signal bandwidth and the incidence angle can improve the cross-track resolution, but since the signal level rapidly drops with increasing incidence angle, this would require much higher transmit power levels. The final output resolution also depends on the number of looks in the processing. The defined number of looks is the number of independent pixels in the unfocused SAR images averaged in the cross-track range and the along-track rather than the number of multiple observations while the satellites travel. If the number of looks is decreased, the resolution improves while the data turns noisier. Fig. 8 illustrates the comparison between the observation resolution of the SSH anomaly achieved by an interferometric swath constellation and that by a conventional altimeter. The reference SSH data are simulated in the same way as in Fig. 5, whereas the smallest scale is about 10 m. In Fig. 8(a), only sparse samples are obtained by a single altimeter satellite, where the observation resolution is more than 1 km in the pulse-limited mode. In contrast, as shown in Fig. 8(b), the interferometric swath altimeter constellation offers observations with a resolution of about 10 m; therefore, from the sampled track, many small-scale SSH features can be observed in the swaths. Finally, from the green region in Fig. 6 and Table II, compared to the comb and specular constellations, interferometric swath constellations can recover finer scales of a few hundred meters in the ocean.

E. SSH Accuracy

Whereas traditional altimeters are optimized for absolute SSH accuracy, swath-observing CubeSat constellations, which are focused on monitoring small-scale features, require merely a good relative SSH accuracy. This is important because it relaxes requirements on, e.g., orbit and atmospheric delay measurements. Relative SSH errors can be contributed by both altimeter noise and systematical errors.

1) *Altimeter Noise*: Altimeter noise is an independent measurement by multiple CubeSats altimeters. It depends on system parameters. For nadir-looking altimeters, we have the following spectrum for altimeter noises [38]:

$$S_n(k_s) = \frac{p^2}{K \left(2 \cdot N \cdot \frac{1}{1+\text{SNR}^{-1}} \right)} k_s \quad (13)$$

where N is the number of independent looks, SNR is the signal-to-noise-ratio, K is the spatial spectrum width which is determined by the along-track sample size and k_s is the spatial wavenumber. A shorter compressed pulselength (larger signal bandwidth), a higher SNR, and more independent looks can improve the accuracy. Generally, the accuracy is not sensitive to the changes of SNR when it is larger than 10 dB.

The altimeter noise spectrum in the interferometric swath constellation is mainly determined by the perpendicular baseline, coherence, and the number of independent looks, which

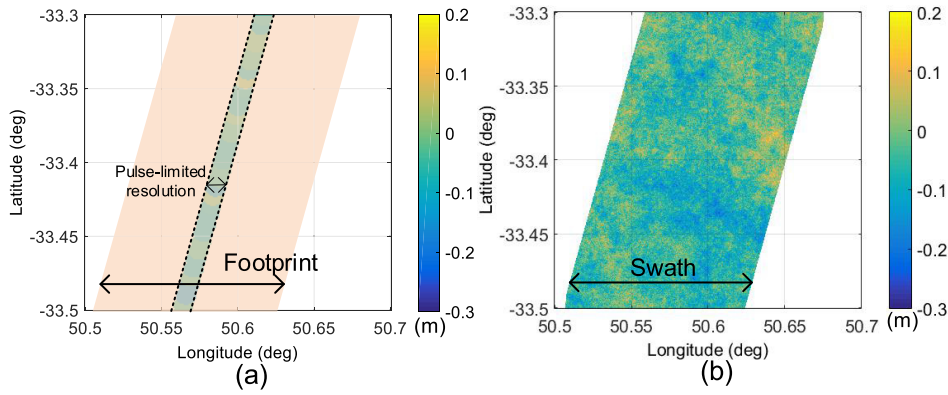


Fig. 8. Comparison of the resolutions of the SSH observations between (a) single pulse-limited altimeter (more than 1-km resolution) and (b) interferometric swath altimeter constellation (about 10-m resolution). We assume both two cases have 0.5-m cross-track antenna sizes.

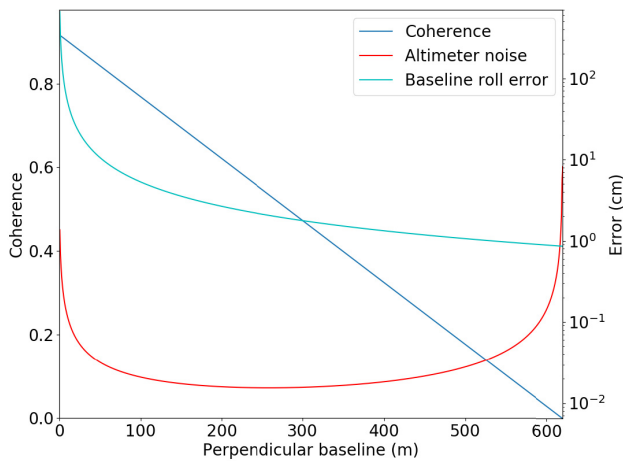


Fig. 9. Coherence, altimeter noise, and baseline roll error as a function of perpendicular baseline in the interferometric swath constellation. We assume a 2° incidence angle is utilized.

can be written as [22], [39]

$$S_n(k_s) = \frac{(R \sin \theta_{\text{inc}} \lambda)^2}{K \cdot (2 \cdot \pi \cdot B_p)^2} \cdot \left(\frac{1 - \gamma^2}{2N \cdot \gamma^2} \right) k_s \quad (14)$$

where R is the slant range, B_p is the perpendicular baseline, and γ is the coherence. It can be noted that a higher coherence in the interferogram, a longer perpendicular baseline, and more independent looks are helpful to reduce the altimeter noise.

The coherence of the interferogram depends on decorrelation sources, such as thermal decorrelation and geometric decorrelation [39]. The geometric decorrelation deriving from the perpendicular baseline between the passive CubeSat (interferometric SAR (InSAR)-pair channels) should be specially considered, which is expressed by

$$\gamma_g = \frac{B_c - B_p}{B_c} \quad (15)$$

where B_c is the critical baseline given by

$$B_c = \frac{2\lambda B_t R \cdot \tan \theta_{\text{inc}}}{c} \quad (16)$$

Fig. 9 shows the performance of the interferometric swath constellation as a function of perpendicular baseline length. A 2° incidence angle is assumed. As shown by the blue

line, the coherence reduces as the perpendicular baseline increases. When the perpendicular baseline is longer than the critical baseline, which is about 620 m, the InSAR pair will be totally decorrelated. At the same time, as altimeter noise also reduces as there is an increase of perpendicular baseline theoretically, as shown by the red line, a nearly 200-m B_p is preferred to achieve the lowest level of the altimeter noise, which can balance both the measurement sensitivity and coherence. Nevertheless, since a large number of looks is applied, the altimeter noise is small even under a low coherence when B_p approaches the critical baseline.

2) *Systematical Error*: Differently, the systematic errors from the multiple measurements in the constellation, such as tropospheric/ionospheric delay, sea state bias (SSB), etc., are correlated spatially; therefore, it is the basis to obtain a high relative SSH accuracy in CubeSat altimeter constellations.

The relative SSH accuracy is analyzed by using the spatial structure functions [39], which is expressed as

$$\sigma_{\text{re}}(\Delta r) = \sigma_{\text{ab}} \sqrt{\left[2 - \frac{2A_R(\Delta r)}{A_R(0)} \right]} \quad (17)$$

where $A_R(\Delta r)$ is the auto-correlation function, σ_{ab} is the Standard deviation of the absolute SSH error, Δr is the spatial distance between the two measurements, and $\sigma_{\text{re}}(\Delta r)$ is the Standard deviation of the relative SSH error. Obviously, the equation indicates that the relative SSH accuracy depends on the absolute SSH accuracy, spatial correlations of the error components, and the separation between the observations of CubeSats.

The absolute SSH accuracy depends on the platform capability and the processing of error corrections on the ground. With respect to an initial design of a CubeSat altimeter in the constellation [30], each altimeter works only in a single-frequency and is equipped with a dual-frequency global positioning system (GPS) and a low size, weight, power, and cost (SWaP-C) star tracker [40]; meanwhile, only the central satellite carries a nadir-looking radiometer. Therefore, the achievable absolute SSH accuracies under different constellations are provided in Table III according to the study in Jason-2 and SWOT [22], [41], [42]. The applied correction in each term is: 1) SSBs are corrected by using

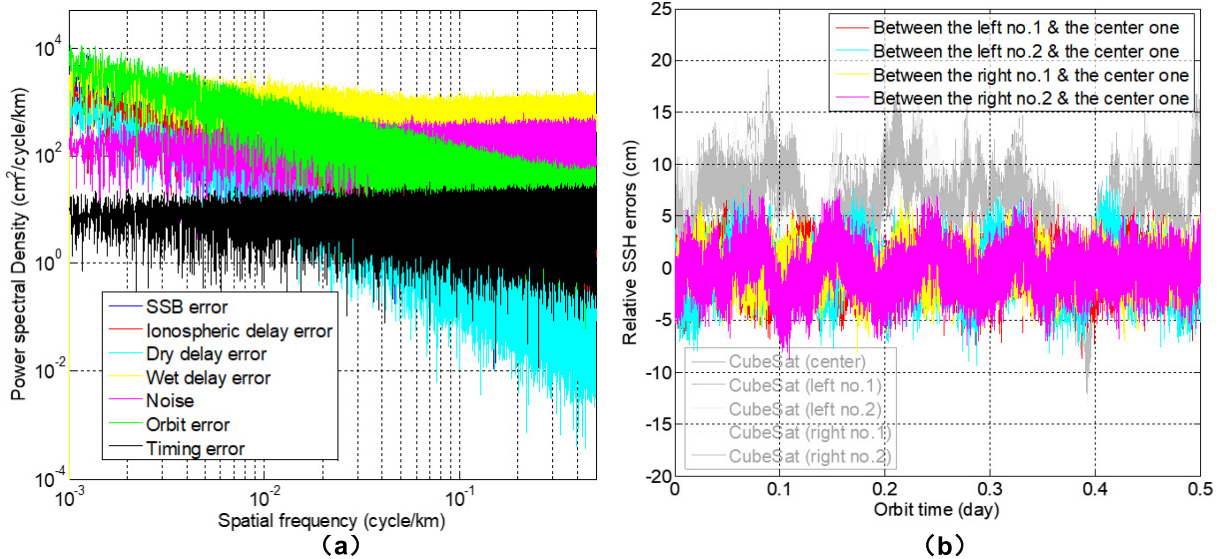


Fig. 10. Spatial spectra of SSH error components and the relative SSH accuracy (half a day). (a) Error spatial spectra with scales from 1 to 1000 km (one random realization). (b) Absolute SSH accuracy (gray lines in the background) and the relative SSH accuracies (colored lines) under the comb constellation case.

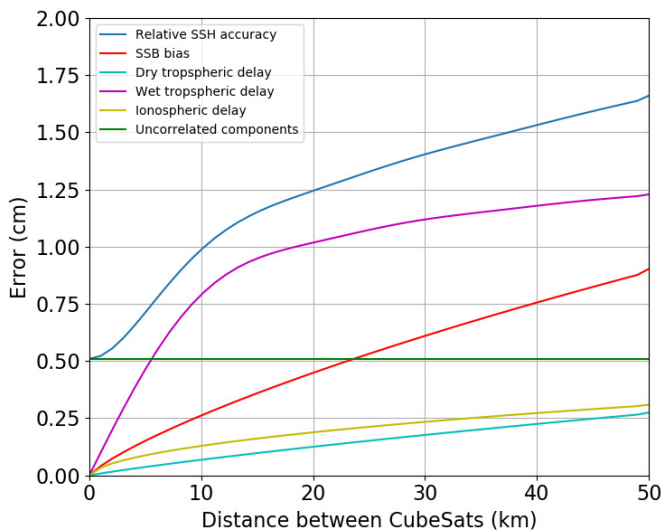


Fig. 11. Relative SSH error components as a function of distance between CubeSats in the comb constellation. The utilized error spatial spectra and absolute SSH errors after corrections are the same as those listed in Table III. The uncorrelated components are the altimeter noise, random timing errors, and relative orbit errors.

the SWH measurements from nadir-looking altimeters and the four-parameter BM4 parametric model; 2) weather model assimilation with the European Center for Medium Range Weather Forecasting (ECMWF) data is used to compensate the dry tropospheric delay; 3) applying the measurements from a nadir-looking radiometer to remove wet tropospheric delays; 4) ionospheric delays are corrected by using a global total electron content data; and 5) the achieved radial orbit accuracy is 5 cm by using a dual-frequency GPS system [43].

The spatial correlations of the error components, represented by the spatial structure functions, can be calculated from the error spatial spectra. To simplify the analysis, we assume that

the error spatial spectra are reciprocal in both along-track and cross-track directions. In this way, a one-dimensional (1-D) spectra can be used to describe the auto-correlation functions, given by

$$A_R(\Delta r) = \text{IFFT}[S(k_s)] \quad (18)$$

where $S(k_s)$ is the error spatial spectrum, and $\text{IFFT}[\cdot]$ is the inverse Fourier transform operator.

SSB, dry, and wet tropospheric delays, ionospheric delays are modeled by the spatial power-law spectra which derive from swath altimeter analyses [22], where their spectral indexes are listed in Table III. Orbit error is a very low-frequency noise along the azimuth, which is modeled by the Gaussian noise with a correlation length of 40000 km along the orbit. Nevertheless, the relative orbit errors between the multiple measurements in the swath-observing altimeter constellations can be considered as the uncorrelated noises with a millimeter-level Standard deviation if the system applies an intersatellite relative navigation formation flying technique [44]. In addition, uncorrelated random timing errors from the drifts in the oscillator frequency are also taken into account.

Fig. 10 shows one realization of these error spatial spectra and the SSH error components in the comb constellation case. Because of the spatial coherence components of the systematical errors from multiple measurements in the constellations, the relative SSH errors are several times lower than the absolute SSH error, as illustrated in Fig. 10(b), implying that the system has a potential to recover the small-scale features with weaker amplitudes.

Besides the spatial error spectra, the distance between CubeSats also determines the relative SSH accuracy between multiple measurements. Fig. 11 illustrates that the relative SSH error increases with the distance between the CubeSats for a comb constellation. The degradation comes from the

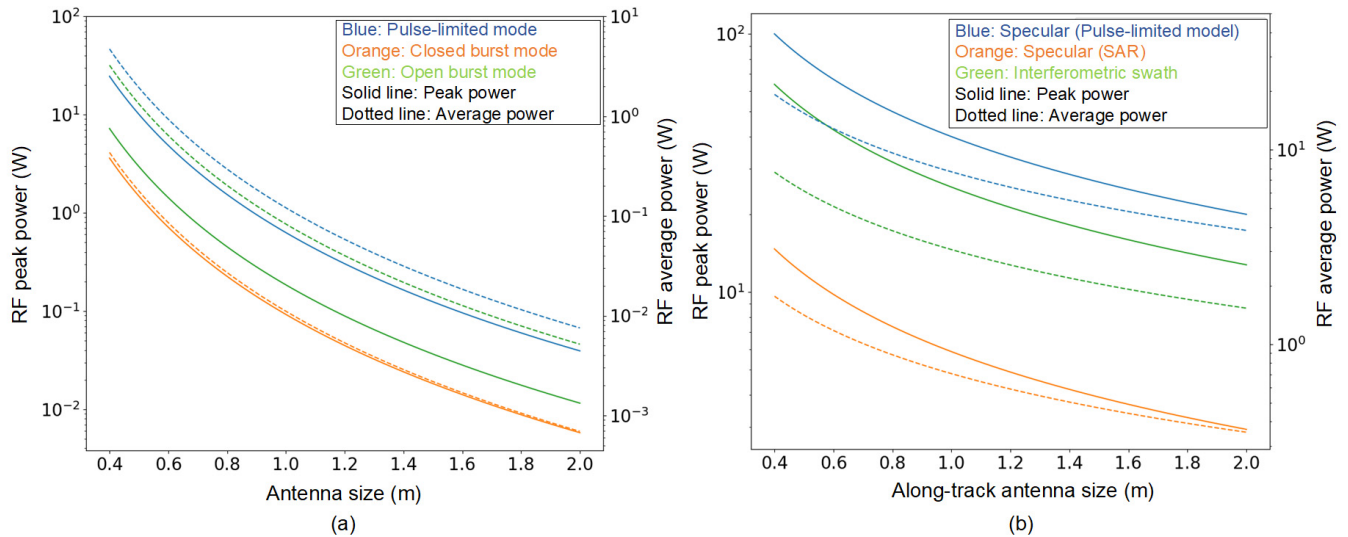


Fig. 12. RF power requirements as a function of antenna size under (a) different operating modes and (b) different constellations. We consider the following conditions in the simulation: 1) the instrumental and atmospheric loss is 7 dB; 2) the power is evaluated for the active CubeSat at the beam edge to satisfy the desired SNR in the bistatic constellations; 3) we use a squared antenna in the monostatic constellations and an elongated antenna with a fixed cross-track dimension of 0.5 m in the bistatic constellations; 4) the uncompressed pulselength in the open burst mode is half of that in the closed burst mode; and 5) a 2° mean incidence angle is used in the interferometric swath constellation.

progressively decorrelated errors from SSB and atmospheric delays when the distance increases. Meanwhile, the uncorrelated components from the altimeter noise, random timing errors, and relative orbit errors are independent of the distance. Therefore, a shorter distance corresponds to a higher relative SSH accuracy, while the drawback is the loss of total swath width. In this view, a careful trade-off about the intersatellite distance in comb constellation should be made. Otherwise, if a too large distance is selected, the errors will be totally independent and the system will lose the advantage for the relative SSH measurement. Accordingly, as for the specular constellation, due to its short distances between different observations, its systematical errors have a high spatial correlation and the relative SSH accuracy in the measurements is good.

It should be specially noted that radial orbit errors in the interferometric swath constellation can produce baseline roll errors, where they will result in a phase slope error in the interferogram and rotate the whole scene [45]. The relative SSH measurement error within the swath from the baseline roll error is expressed as

$$\Delta e_r = \frac{\lambda h}{2D} \cdot \frac{\Delta B_{\parallel}}{B_p} \quad (19)$$

where ΔB_{\parallel} is the parallel baseline error.

SSH measurement errors from baseline roll angle errors are usually very large. To decrease ΔB_{\parallel} is a basic way to reduce the error, while it depends much on the improvement of positioning knowledge. A longer B_p (see the light blue line in Fig. 9) and a larger antenna (result in a smaller swath size) can also help to decrease the baseline roll error, which will pose higher system requirements and reduce the observation performance. If a coherence of 0.5 is assumed, corresponding to a nearly 300-m B_p under a 2° incidence angle case, and

the ΔB_{\parallel} is 1 mm, the relative SSH error through the whole swath is nearly 1.8 cm.

Finally, the overall SSH measurement accuracies have been summarized in Table III. In our studied cases, the comb constellation can be achieved a less than 2-cm relative SSH accuracy between the nearby CubeSats. Owing to a shorter intersatellite distance, the relative SSH accuracy of the specular constellation is only one-third of that in the comb case, which is less than 0.6 cm. As we discussed previously, the large baseline roll error is the dominant error component for the interferometric swath constellation. Besides requiring a more accurate positioning technique, we also need to compromise between some system parameters (e.g., swath size, incidence angle) and the performance to reduce the error.

IV. SYSTEM REQUIREMENT ANALYSIS

Section III provides the performance analyses of different CubeSat altimeter constellations. In addition, because CubeSats generally provide limited accommodation space, power, and mass for the onboard instruments, we analyze the system requirements in this section, which should satisfy the implementation boundary conditions of a typical CubeSat, for example, no larger than 12U. The system parameters for the analysis are listed in Table I.

A. RF Power and Antenna

Requirement analysis of RF power and antenna is very basic in the altimeter payload system analysis. The analysis is conducted based on a flat ocean surface assumption. The required power can be calculated from the well-known radar equation [47]

$$P_t = \frac{4\pi^3 \cdot R^4 \cdot \text{SNR} \cdot k_B \cdot T \cdot B_t \cdot F \cdot L_{\text{atm}}}{G^2 \lambda^2 \sigma} \quad (20)$$

TABLE III

SSH ACCURACY ANALYSIS OF DIFFERENT CONSTELLATIONS. (p IS THE SPECTRAL INDEX OF THE ERROR SPATIAL SPECTRUM; THE SYSTEMS OPERATE UNDER A PULSE-LIMITED MODE; ALL RELATIVE ERRORS IN THE COMB AND SPECULAR CONSTELLATIONS ARE THE ERRORS BETWEEN THE NEARBY CUBESATS AND THE ABSOLUTE ERRORS ARE FROM THE CUBESATS IN THE CENTER OF THE CONSTELLATIONS)

Error sources	Accuracy (cm)	Comb constellation	Specular constellation	Interferometric swath constellation
Altimeter noise	Absolute		0.35 ^{*1}	0.01 ^{*11}
	Relative		0.50	
Sea state bias delay	Absolute ^{*2}		2.0	0.06 ^{*3}
	Relative ($p = -8/3$)	0.90	0.07	
Dry tropospheric delay ^{*4}	Absolute		0.7	0.02
	Relative ($p = -3$)	0.27	0.02	
Wet tropospheric delay ^{*5}	Absolute		1.2	0.21
	Relative ($p = -1.8 \& 0.8$)	1.23	0.20	
Ionospheric delay ^{*6}	Absolute		0.5	0.001
	Relative ($p = -2.1$)	0.31	0.05	
Orbit radial error	Absolute ^{*7}		5	1.77 ^{*8,11}
	Relative ^{*9}	0.09	0.06	
Timing error ^{*10}	Absolute	0.02	0.03	0.003
	Relative		0.03	
Total noise	Absolute		5.60	-
	Relative	1.66	0.55	1.78

^{*1} It considers a 7.5 km along-track grid size (1 second averaging) in the data processing of traditional altimeters; ^{*2} It is under a case of 2 m SWH; ^{*3} It is corrected by the nadir-looking measurements; ^{*4} It is corrected by the Chelton model; ^{*5} It conducts the correction from the nadir-looking radiometer measurements; ^{*6} It is corrected by using Ionex model [46]; ^{*7} It uses a dual-frequency GPS; ^{*8} The error is mainly from the baseline roll error; ^{*9} It is assumed that the system obtains a 1mm relative positioning accuracy by using an inter-satellite relative navigation formation flying technique [44]; ^{*10} The timing synchronization accuracy is 10^{-10} ; ^{*11} The considered incidence angle is 2° and the baseline is 300 m under a coherence of 0.5. The grid size is 1 km.

where P_t is the transmit power, k_B is the Boltzmann's constant, T is the temperature, F is the receiver noise figure, L_{atm} is the atmospheric attenuation, G is the antenna gain, and σ is the radar cross section.

Fig. 12(a) provides the required RF power as a function of the size of the squared antenna for monostatic altimeters under different operating modes. Both the pulse-limited mode and two SAR modes (the closed burst and the open burst modes) are considered. The chronograms of these two SAR modes are shown in Fig. 13. It can be seen that the required RF powers are not large in the studied cases. If we design a CubeSat less than 12U and take the proportion of the stowed parabolic antenna in the Raincube design (i.e., a 1.5U stowed antenna for a 6U CubeSat) into account [24], the accommodation space of the antenna should be less than 3U. In this view, a moderate antenna size, typically 0.8 m with a margin of 25%, is recommended for CubeSats to reduce the peak power and the antenna volume. In this case, a 1.5-W RF peak power and a 0.3-W RF average power can satisfy the requirements. SAR mode requires less power compared to the pulse-limited one due to the coherent gain of SAR processing, but it will raise the requirement on the system data rate and onboard computation burden. To reduce the power requirement, the closed burst mode is preferred over the open burst mode, except in the case where a high along-track resolution is demanded.

For the specular constellation, because its swath width is limited by the beam footprint, we prefer an antenna short in the cross-track direction but elongated in the along-track direction to both achieve large swaths and keep the desired antenna gain. To obtain a 10-km swath, an antenna of 0.5 m in cross-track direction is required with the selected orbit height.

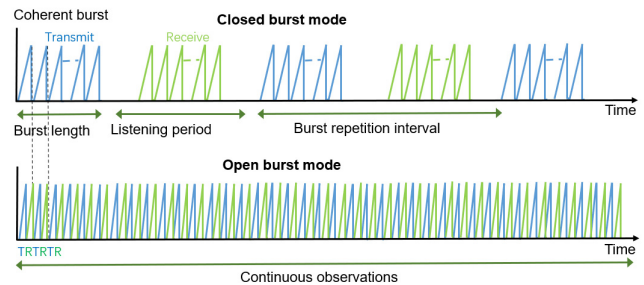


Fig. 13. Chronograms of the closed burst mode and the open burst mode.

The along-track antenna dimension can increase to compensate for the loss of gain due to a reduced cross-track antenna size, which can be up to about 1 m for a less than 3U stowed space. On the other hand, as shown in Fig. 14, where the altimeter noise is calculated as a function of the along-track antenna size based on the number of useful Doppler bins [48], the along-track dimension cannot be longer than 2 m to suppress altimeter noise under the SAR mode. Otherwise, the achieved number of independent observations reduces due to its limitation from the footprint size rather than the Raney size. In addition, as shown in Fig. 12(b), compared to the comb constellation, a higher power is required in the specular constellation because we should compensate the loss of antenna gain and backscatter power even at the edge of the beam illumination area to keep the desired SNR.

Like the specular constellation, we also prefer to implement the elongated antenna to increase swath width in the interferometric swath constellation. Its along-track antenna dimension

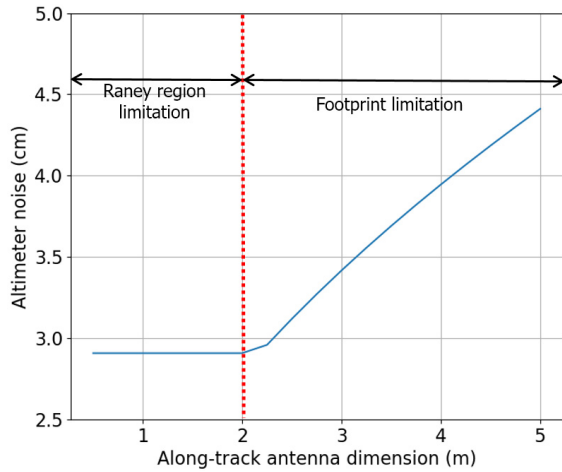


Fig. 14. Relationship between the along-track antenna dimension of the CubeSat and the altimeter noise under an SAR mode (a resolution cell).

also should not be very long to keep a good along-track resolution when the data are fully focused. A 0.5 m (cross-track) \times 1 m (along-track) antenna can obtain a 10-km swath and an optimal along-track resolution of 0.5 m. Compared to the power requirement in other cases, the RF power requirement in the interferometric mode increases due to an off-nadir geometry. The required power goes up quickly as the backscatter coefficient decreases obviously when the off-nadir angle increases. Referring to the Ulaby model [49], we follow the exponential function to calculate the variation of the off-nadir backscatter coefficient. To maintain the required SNR at the far range for the elongated antenna case, the required peak power will be nearly 30 W under a 2° incidence angle as shown in Fig. 12(b).

Overall, the comb and the short-revisit constellations require the lowest RF powers, which operate in the monostatic modes. The 0.8-m square or circular aperture is recommended. For both the specular and the interferometric swath constellations we need a higher power and an elongated antenna. Assuming the RF power generation efficiency is, e.g., 30% and being evaluated through an average dc power consumption, the required total average powers will be less than 30 W for the specular constellation and the interferometric swath constellation, when a 0.5 m (cross-track) \times 1 m (along-track) antenna is implemented, which can be satisfied by power buses on CubeSats [50]. Nevertheless, the entire power bus at Ka-band may be more complex, heavier, and higher cost, where even power transistors in parallel are required to achieve the desired power.

B. Data Rate and Downlink

Supposing we utilize dechirp on receive, the data rate of CubeSat altimeters depends on the system parameters, such as the burst interval time and the number of coherent pulses in the processing. The raw data rate after range compression is expressed by

$$D_r = \alpha \frac{n_r Q_n}{10^6} [\text{Mbps}] \quad (21)$$

where $\alpha = n_p/T_b$ under the pulse-limited and SAR closed burst modes and $\alpha = \text{PRF}$ under the open burst mode, n_p is the number of coherent pulses in the processing, T_b is the burst interval time, n_r is the number of range bins, and Q_n is the number of quantized bits.

After the onboard SAR processing and multilooking (the power summation of range profiles), the data rate reduces to

$$D_p = \frac{n_o n_r Q_n}{10^3} [\text{Kbps}] \quad (22)$$

where n_o is the altimeter observations per second after processing, $n_o = (v_s/\rho_a)$ in SAR mode and relates to the number of integrated looks in the pulse-limited mode.

We consider using 8-bit samples in both I and Q channels for the raw data, 128 range samples in each observation, and four observations per second in the traditional mode after onboard processing. According to the parameters in Table I, the data rates under different operating modes are given in Table IV. It can be seen that the SAR mode leads to a higher data rate after processing because a higher resolution results in a higher number of altimeter observations per second. In the case of the interferometry configuration, the data rate has to be doubled due to its two channels if the interferometric processing is on the ground.

In all cases, data rate highly depends on the onboard processing. Fig. 15 shows the data flow of the CubeSat altimeter constellations. The operations in the onboard processing module are described in the gray block, where onboard tracking based on digital elevation models, preliminary calibrations and corrections for signal's power and range, range compression, multilooking, and some SAR processing are included. After onboard processing, the data rate is reduced to a kbps-level from the Mbps-level. Then, the data is transmitted to the ground station for retracking and further calibration and correction for instrument errors, atmospheric delays, etc. For the interferometric swath constellation, interferometric processing can be done onboard to reduce the data rate to only less than 12 kbps, as illustrated by the block on the right-hand side in Fig. 15. However, since the interferometric channels are separated on two CubeSats, we need an intersatellite link to transmit the focused data from the slave CubeSat to the master one.

To realize the onboard processing within the SWaP-C goal on CubeSat platforms, we propose to use a commercial low-power and low-cost field-programmable gate array (FPGA), such as the Xilinx Artix-7 family, with low power consumption from 1 to 2.5 W [51]. A large variety of components is available in this family [e.g., digital signal processor (DSP) slices and block random access memories (RAMs)] for onboard fast Fourier transform (FFT), inverse FFT (IFFT), and matrix hadamard product operations. The targeted time-consumption to process the received data per orbit is from minute-level to less than the full standby period of the transmitter. The entire printed circuit board (PCB) with an aforementioned FPGA for the digital and processing unit will be designed in a SWaP-C manner, which can be achieved with a size of less than 0.4U and a weight of less than 2 kg [52]. The currently available

TABLE IV
DATA RATE AND DOWNLINK REQUIREMENTS UNDER DIFFERENT WORK-
ING MODES

Mode	Raw data rate (Mbps)	Processed data rate (kbps)	Downlink* ¹ (GB)
Pulse-limited	8.2	8.2	0.7
SAR	Closed burst	23.5	2.1
	Open burst		
Interferometry	-	47.0* ² 11.8* ³	1.8* ² 0.4* ³

*¹ Data downlink to the ground only after on-board processing for five CubeSats. The interferometric swath constellation has one nadir-looking channel and two interferometric channels; *² interferometric processing is on the ground; *³ an inter-satellite link is implemented and the interferometric processing is on-board.

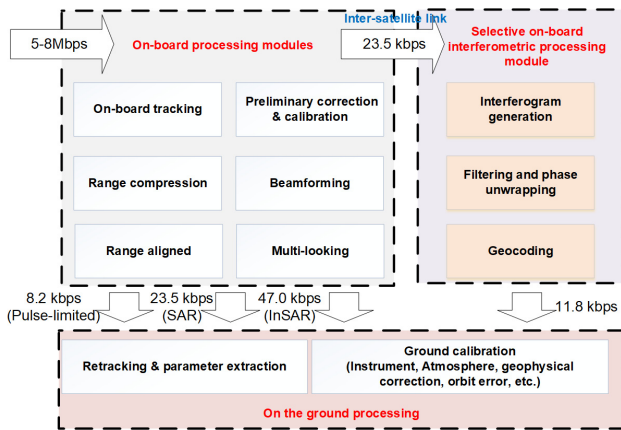


Fig. 15. Data flow of the CubeSat altimeter constellations.

capabilities offer sufficient confidence that a suitable solution can be achieved in the mission design phase.

The data downlink requirement is then estimated by the data output per week under an operation duty cycle of 25%, which is listed in Table IV. It should be noted that in the operation phase only onboard processed data downlink is foreseen. Nevertheless, some but not all raw data can be downloaded for testing and to verify the effectiveness of the onboard processing algorithms. The maximum required downlink data of the payload is nearly 2 GB/week, which is feasible by the current data downlink techniques used in CubeSat platforms [53]. Some strategies can be utilized to further reduce the data downlink burden, such as by transmitting preprocessed “low-resolution” data from onboard processing and reducing the quantized bit number.

C. Synchronization

Synchronization is the key issue for bistatic altimeter constellations. Only timing synchronization is required for the specular constellation if the system operates in the pulse-limited mode. In this case, the requirement of time synchronization accuracy is generally tenth of the compressed pulse [54], which is given by

$$\sigma_t = \frac{1}{20B_t \cdot t_u} \quad (23)$$

where t_u is the update rate of the clocks. According to the system parameters in Table I and assuming an update rate of the clock is 1 Hz, the required time stability is 0.1 ns.

A phase synchronization should be considered in the specular constellation under the SAR mode and the interferometric swath constellation. The required stability of the oscillator to obtain the required phase synchronization is written in [54]

$$\sigma_{os} = \frac{\phi_e}{2\pi f_0 T_{int}} \quad (24)$$

where ϕ_e is the maximum phase error, f_0 is the carrier frequency, and T_{int} is the coherent time. Assuming ϕ_e is $\pi/4$ under the unfocused SAR processing and we integrate ten coherent pulses over 0.5 ms, the required stability for the oscillator is about 1.3×10^{-8} . The required stability in the interferometric swath constellation is higher than that in the specular constellation. If we integrate the signal over 35 ms to obtain a 10-m resolution in azimuth and the maximum phase noise is 3.6° , our desired oscillator stability is nearly 8×10^{-12} .

These timing and phase synchronization requirements can be satisfied by using some disciplining stable local oscillators for CubeSat platforms, which can achieve stability at a level of 1×10^{-13} [55]. Such a high stable oscillator can not only satisfy the requirement for phase synchronizations but also can support the timing synchronization. With the oscillator, 1 pulse-per-second signal (PPS) GPS synchronization could deliver an initial timing synchronization accuracy of even 3 ns between two CubeSats [54], [56]. Since the oscillator is highly stable for a long time compared to our timing synchronization requirement, we can then estimate the timing differences between CubeSats by averaging the data for a period of time and correct the measurements. Assuming a 1×10^{-13} frequency stability of the oscillator and a stable ocean surface over hundreds of kilometers, for example, the timing drift from the oscillator over an integrated time of 100 s is only 0.01 ns, which is well within the required timing synchronization accuracy. Besides, some further corrections can also be done on the ground with the help of the cross-check measurements from other altimeters.

D. Formation Control

Relative orbit knowledge and control accuracies are important for satellite formation missions. Similarly, for radar altimeter constellations, the relative orbit knowledge accuracy is essential to achieve a high relative SSH accuracy as explained in Section III. Generally, global navigation satellite system (GNSS) measurements are the typical source for relative navigation which can provide sub-meter root mean square (rms) accuracy in three dimensions [57]. It is also suggested that sub-millimeter accuracy is achievable with a dual-frequency GPS combined with a star tracker [44].

Regarding the relative orbit control, its accuracy requirement depends on the geometry of an orbit constellation. Among all the constellations, the interferometric swath constellation requires more stringent orbit control due to its close formation flying configuration of the interferometric CubeSat channels. First, as the cross-track distance goes to zero at the poles, either the radial or along-track position

component has to be nonzero, and it requires periodic relative orbit maneuvering to avoid collisions between CubeSats. On the other hand, we need to design the passive CubeSat interferometric channels to work in a stable interferometric observation geometry, for example, e.g., a HELIX formation. In this case, we consider applying the tighter formation control method, that applied in TanDEM-X [58]. It used the well-known eccentricity/ inclination vector separation scheme that counters the J2 perturbation caused by Earth oblateness over the lifetime [59], [60]. We desire a cross-track and an along-track control accuracy requirements of, respectively, 30 m (rms) and 200 m (rms) [61], which can satisfy the baseline requirement of about 300 m to sustain a geometric coherence higher than 0.5 under a 2° incidence angle.

For other close formation flying cases, a specular constellation and a comb constellation with small intersatellite distances, the defined formation control accuracy requirements are 60 m (rms) in the cross-track and 400 m (rms) in the along-track, assuming a safe distance of 100 m, which is sufficient due to only an objective of safety distance keeping in these systems. In these cases, we adopt another formation-keeping strategy recently proposed in [62], which counters only the differential drag perturbation not the J2 perturbation so that it reduces the formation-keeping burden on CubeSats but still guarantees collision avoidance between satellites. The orbit control accuracies in the comb constellation with large intersatellite distances and the short-revisit constellation can be much less stringent thanks to their low collision probability. It should also be noted that the along-track control requirement is generally larger than the cross-track control requirement, because bounding the along-track error is much harder than the cross-track error due to the large uncertainty in the atmospheric drag model that decides how fast the satellite velocity gets slow down.

E. Delta-v Cost

The delta-v budget analysis is important to confirm that a space mission is sustainable for the designed lifetime for the given propellant mass [63]. In particular, since satellites with a CubeSat form factor lack orbit control capability, analyzing the delta-v cost in the early development phase is essential for mission performance evaluation.

Five orbit maneuvering tasks necessary for typical formation flying missions are: 1) initial reference orbit correction; 2) initial formation acquisition; 3) periodic orbit maintenance; 4) periodic formation-keeping; and 5) contingencies. Briefly introducing each of the tasks, the first two tasks are conducted at the mission start while the first is to correct the orbit injection error generated by a launcher and the second is to distribute the satellites into their designated orbits. The other tasks are either periodically or irregularly conducted across the mission lifetime. The third task is to compensate for the altitude loss, and the fourth task is to keep the constellation orbits against the orbit perturbations while the last task is for emergency when being switched to a safe mode due to anomaly.

TABLE V

DELTA-V REQUIREMENT FOR DIFFERENT CONSTELLATIONS (THE LARGEST DELTA-V AMONG THE SATELLITES)

Constellation	Delta-v required (m/s)		
	500 km	600 km	650 km
Cross-track comb	35.8	35.2	36.1
Specular	49.3	36.5	35.0
Interferometric swath	58.3	45.5	44.0
Along-track comb and short-revisit	20.0	16.9	16.4

Table V summarizes the largest required delta-v among the satellites for the five constellations at three orbit altitudes. Two assumptions made for the analysis are that the satellites are already inserted into their designed orbits by a launcher, and the periodic orbit maintenance is turned off for delta-v reduction (of approximately 10 m/s at 634-km altitude over 1.5 years) in trade-off of a time-varying revisit period property. It can be seen that the along-track comb has an advantage over the cross-track comb thanks to flying on the same orbit plane which exerts similar orbit perturbations among satellites. The specular and interferometric constellations require the larger delta-v due to the differential drag between an active satellite and passive satellites from the difference in ballistic coefficients. Applying a tighter formation control in the interferometric swath constellation makes its required delta-v the largest one among all the constellations.

It should also be noted that the considered delta-v budgets do not include the delta-v cost in the active deorbiting, although it is possible to use the remaining propellant to do this. Instead of active deorbiting using propulsion or drag devices, we decided to utilize the natural decay strategy for deorbiting. The reference orbit selection (<650 km) and the relatively large surface/mass ratio make sure the satellite will decay to the atmosphere and burn there within 25 years after lifetime even under the worst scenario.

V. TECHNOLOGY READINESS ASPECTS FOR CUBE-SAT ALTIMETER SYSTEMS

A. Deployable Antennas

Deployable antennas are one of the important parts for the implementation of CubeSat altimeter constellations. We desire a larger antenna to obtain enough antenna gain, while they should occupy a small space and be light. According to the latest antenna techniques, folded panel reflectarray antennas, inflatable antennas, and mesh reflector antennas are proper designs for CubeSats [64], [65]. They have different advantages in deploy capability, surface accuracy, efficiency, etc. Some of them have already worked in space and perform well. Nevertheless, besides further work to increase stowed efficiency, we should also need to develop deployable elongated antennas for specular and interferometric swath constellations. It seems that it can be built from a frame of reflectarray antennas. However, some work should be refined to improve the efficiency and to adapt an antenna with a large along-track dimension in space.

TABLE VI

SYSTEM PERFORMANCE AND REQUIREMENT COMPARISON OF DIFFERENT CONSTELLATIONS. GREEN: ADVANTAGES; BLUE: FAIR; ORANGE: SOME LIMITATIONS

Property	Constellation				Short-revisit
	Swath-observing altimeter				
	Cross-track comb	Along-track comb	Specular	Interferometric swath	
Swath size	Up to hundreds of km		~30 km	~10 km	-
Spatial sampling density	Local	Down to km		Down to 10 m	-
	Global	No gap	~60 km gap	~80 km gap	~90 km gap
Revisit	days		days	days	hourly
Relative SSH accuracy	Down to sub-centimeter		Down to sub-centimeter	Mainly determined by baseline roll error	-
Cross-track Resolution	km		km	Down to 10m	km
System requirement	<ul style="list-style-type: none"> •Low power •Simple antenna 	<ul style="list-style-type: none"> •Low power •Simple antenna •Small delta-v requirement 	<ul style="list-style-type: none"> •High power •Complex antenna •Synchronization 	<ul style="list-style-type: none"> •High power •Complex antenna •Synchronization •High formation control requirement •High relative positioning accuracy requirement 	<ul style="list-style-type: none"> •Low power •Simple antenna •Small delta-v requirement

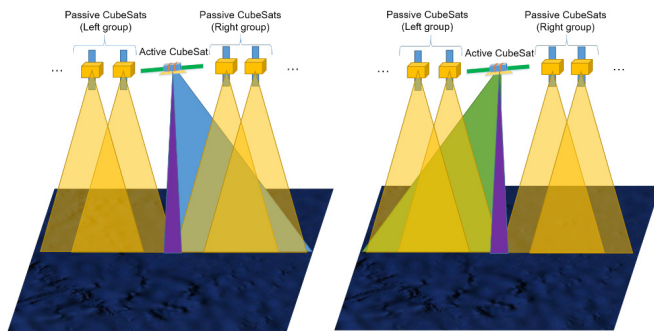


Fig. 16. Concept of a CubeSat altimeter constellation with DBF. Blue beam: right-looking beam; purple beam: nadir-looking beam; green beam: left-looking beam.

B. Swath Extension by Digital Beamforming (DBF)

A limited footprint is a big drawback for specular and interferometric swath constellations. A possible way to solve the problem is to develop a beam-steering antenna by using DBF. The DBF concept in the application is described in Fig. 16. For simplicity, we consider doubling the swath length. The passive cubsats are allocated as the left and the right groups in terms of their relative position toward the active sensor. Then, we can conduct the interleaved transmit mode by right-looking, nadir-looking, and left-looking. During the listening periods, the active CubeSat can also receive the echo from the nadir tracks. When realizing it, a long phased array antenna can be implemented to achieve the narrow beam for the nadir-looking, and two small parts of the antenna in the left and right sides, respectively, can be activated in turn to double the off-nadir swath observations.

C. Relative Orbit Knowledge Accuracy

As we discussed in Section III, relative orbit knowledge accuracy is a basic limitation factor to improve the relative SSH accuracy in the interferometric swath constellation. If an objective relative SSH error from the baseline roll error is smaller than 1 cm under a 300-m perpendicular baseline, the required relative orbit error in radial should be about 0.5 mm. So far, it is still impossible for the current intersatellite

relative positioning technique to realize it, where the best accuracy is about 0.7 mm [44]. For the application scenarios with smaller baselines, we will require even finer accuracy. In addition, more related experiments about the achievable relative positioning accuracy should also be tested on the CubeSat platforms.

D. Miniaturized and Low-Cost Radiometers

Miniaturized and low-cost radiometers are expected to be developed. Some important work has already been done by the Radiometer Atmospheric CubeSat Experiment (RACE) system to raise the technology readiness level (TRL) of CubeSat radiometers, which only require a 1.5U volume [66]. Lighter and cheaper radiometers can enable more CubeSats in the constellation to have radiometers, allowing a more accurate correction of wet tropospheric delays through the whole swath. It could be concluded from Table III that a single nadir-looking radiometer on the center CubeSat for a large swath is not sufficient. Only for the small swath cases, no radiometers onboard can be acceptable as it leads to a slightly degraded relative SSH accuracy. Alternatively, one could think of not set up the constellation with large separations between CubeSats.

VI. SYSTEM SUMMARY AND COMPARISON

Table VI shows the summary of performances and system requirements for different CubeSat altimeter constellations. It can be concluded that comb and specular constellations mainly aim at observations of mesoscales in the ocean. Comb constellations can observe a large swath due to their good global spatial sampling performance. To observe sub-mesoscales or near-shore regions, an interferometric swath constellation is preferred to achieve a much finer cross-track resolution. Although both the specular constellation and the interferometric swath constellation can observe small features in the ocean, they can only monitor small swaths. For weather forecasting and observations of some quick interactions between currents and waves, a short-revisit constellation has the advantage to achieve hourly revisits, but many CubeSats are required in different orbit planes. Note

that the short revisit constellation principle can be applied to any of the other constellations. Since all the CubeSats are the same, comb and short-revisit constellations are relatively simple and cost-saving as it does not require to design different platforms and to arrange inter-CubeSats cooperations. Both specular and interferometric swath constellations have high requirements on power, antenna design, and synchronization. On the other hand, only receivers are required for the passive CubeSats, which makes these platforms simpler to construct and more affordable. An interferometric swath constellation needs more effort to be built due to its high requirements on formation control and relative positioning accuracy. Some of these requirements can be addressed by an enhanced CubeSat platform or even a microsat, such as the high power and complex antennas, where more powerful instruments can be implemented. Nevertheless, to achieve sufficient formation control capability and acceptable relative orbit accuracy still needs some effort.

VII. CONCLUSION

We presented the performance analysis and methodology for CubeSat altimeter constellations. These altimeter constellation concepts can break the spatial-temporal observation limitations in oceanographic applications.

A swath-observing altimeter constellation can be realized by the comb, specular, or interferometric swath configurations, which aims for the observations of the relatively small mesoscale and sub-mesoscale eddies, currents, and waves in the open ocean. The comb constellation has a flexible structure in which the distance between the CubeSats and the observation swath can be tuned according to observation objectives. In contrast, the observation region and the distance of the CubeSats in the specular constellation are limited by its footprint. Therefore, the comb constellation has a better capability to observe large regions. As for the local sampling, the performances are dictated by the resolution of the sensors and the distances between the sensors in both two constellations. To observe finer features in the open ocean or coastal regions, an interferometric swath constellation is required. A short-revisit constellation with many CubeSats distributed along different orbit planes and phases is the only way to shorten the repeat cycle below 24 h.

In particular, good spatial and temporal sampling performances can be expected if the building blocks for short revisit constellations are swath-observing constellations rather than single sensors. Besides the good sampling performance, our study shows that although the absolute SSH accuracies are limited compared to large altimeter satellites, the relative SSH accuracy of the CubeSat altimeter constellations is very good, because the systematical errors are spatially correlated and will partly cancel out. Shorter distances between the observation samples achieve smaller relative SSH errors.

Finally, the study suggests that CubeSat altimeter constellations are promising concepts that can achieve enhanced performance for different oceanic applications compared to large-satellite altimeters.

The implementations of different constellations pose different system requirements, which should be achievable by

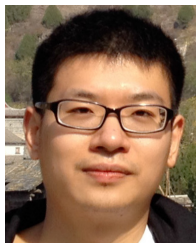
CubeSats. The comb and the short-revisit constellations are relatively easy to realize with CubeSats owing to the current readiness levels of the required technology and because the systems are identical and operate independently, without precise synchronization; thus, they almost have no rigor limitations in their implementations. The specular constellation is more complex, first of all but not only due to the more stringent requirements on high power, synchronization, and deployable antennas. For the interferometric swath constellation, additional complexity is formed by the high formation control requirement and the required relative positioning accuracy which is very hard to achieve. Using an enhanced platform as the active platform is a possible solution in these bistatic configurations to address high system requirements. Besides, we still look forward to the development of CubeSat techniques to conquer the limitations in swath sizes and accuracies, such as by using a DBF technique on CubeSats. At that time, CubeSat altimeter constellations can achieve better performance and become more efficient, which can support more advanced studies in oceanic applications.

REFERENCES

- [1] E. J. Walsh, "Analysis of experimental NRL radar altimeter data," *Radio Sci.*, vol. 9, nos. 8–9, pp. 711–722, 1974.
- [2] Y. L. Roy, M. Deschaux-Beaume, C. Mavrocordatos, M. Aguirre, and F. Heliere, "SRAL SAR radar altimeter for sentinel-3 mission," in *Proc. IEEE Int. Geosci. Remote Sens. Symp.*, Barcelona, Spain, Jul. 2007, pp. 219–222.
- [3] C. Francis, "CryoSat mission and data description. Technical document," European Space Agency (ESA), Paris, France, Tech. Rep. CS-RP-ESA-SY-0059, 2007.
- [4] P. Tandeo, P. Ailliot, B. Chapron, R. Lguensat, and R. Fablet, "The analog data assimilation: Application to 20 years of altimetric data," in *Proc. 5th Int. Workshop Climate Informat.*, Sep. 2015, pp. 1–2.
- [5] R. S. Nerem, B. D. Beckley, J. T. Fasullo, B. D. Hamlington, D. Masters, and G. T. Mitchum, "Climate-change-driven accelerated sea-level rise detected in the altimeter era," *Proc. Nat. Acad. Sci. USA*, vol. 115, no. 9, pp. 2022–2025, Feb. 2018.
- [6] F. Boy, J.-D. Desjonqueres, N. Picot, T. Moreau, and M. Raynal, "CryoSat-2 SAR-mode over oceans: Processing methods, global assessment, and benefits," *IEEE Trans. Geosci. Remote Sens.*, vol. 55, no. 1, pp. 148–158, Jan. 2017.
- [7] S. Vignudelli, A. G. Kostianoy, P. Cipollini, and J. Benveniste, *Coastal Altimetry*. Berlin, Germany: Springer, 2011.
- [8] D. B. Chelton and M. G. Schlax, "Global observations of oceanic Rossby waves," *Science*, vol. 272, no. 5259, pp. 234–238, Apr. 1996.
- [9] D. B. Chelton, R. A. deSzoeke, M. G. Schlax, K. El Naggar, and N. Siwertz, "Geographical variability of the first baroclinic Rossby radius of deformation," *J. Phys. Oceanograph.*, vol. 28, no. 3, pp. 433–460, Mar. 1998.
- [10] J. Gula, *Mesoscale and Submesoscale Turbulence in the Presence of Topography*. Brest, France: Universit  de Bretagne Occidentale, 2020.
- [11] J. Callies, R. Ferrari, J. M. Klymak, and J. Gula, "Seasonality in submesoscale turbulence," *Nature Commun.*, vol. 6, no. 1, pp. 1–8, Nov. 2015.
- [12] J. Gula, M. J. Molemaker, and J. C. McWilliams, "Topographic generation of submesoscale centrifugal instability and energy dissipation," *Nature Commun.*, vol. 7, no. 1, pp. 1–7, Nov. 2016.
- [13] R. Ferrari and C. Wunsch, "Ocean circulation kinetic energy: Reservoirs, sources, and sinks," *Annu. Rev. Fluid Mech.*, vol. 41, no. 1, pp. 253–282, Jan. 2009.
- [14] S. K. Dube *et al.*, "Storm surge modeling and applications in coastal areas," in *Global Perspectives on Tropical Cyclones: From Science to Mitigation*. Singapore: World Scientific, 2010, pp. 363–406.
- [15] D. Chelton, J. Ries, B. Haines, L. Fu, and P. Callahan, "Satellite Altimetry," in *Satellite Altimetry and Earth Sciences: A Handbook for Techniques and Applications*, L.-L. Fu and A. Cazenave, Eds. New York, NY, USA: Academic, 2001.

- [16] R. K. Raney and D. L. Porter, "WITTEX: An innovative three-satellite radar altimeter concept," *IEEE Trans. Geosci. Remote Sens.*, vol. 39, no. 11, pp. 2387–2391, Nov. 2001.
- [17] E. Rodriguez, D. Esteban Fernandez, E. Peral, C. W. Chen, J.-W. De Bleser, and B. Williams, "Wide-swath altimetry: A review," in *Satellite Altimetry Over Oceans and Land Surfaces*, vol. 2. Boca Raton, FL, USA: CRC Press, 2018.
- [18] P. Cipollini, F. M. Calafat, S. Jevrejeva, A. Melet, and P. Prandi, "Monitoring sea level in the coastal zone with satellite altimetry and tide gauges," *Surv. Geophys.*, vol. 38, no. 1, pp. 33–57, 2017.
- [19] J. Gula, M. J. Molemaker, and J. C. McWilliams, "Submesoscale cold filaments in the Gulf stream," *J. Phys. Oceanogr.*, vol. 44, no. 10, pp. 2617–2643, Oct. 2014.
- [20] M. Martin-Neira, C. Mavrocordatos, and E. Colzi, "Study of a constellation of bistatic radar altimeters for mesoscale ocean applications," *IEEE Trans. Geosci. Remote Sens.*, vol. 36, no. 6, pp. 1898–1904, Nov. 1998.
- [21] R. Morrow *et al.*, "Global observations of fine-scale ocean surface topography with the surface water and ocean topography (SWOT) mission," *Frontiers Mar. Sci.*, vol. 6, p. 232, May 2019.
- [22] D. Esteban-Fernandez, *SWOT Project Mission Performance and Error Budget Document*, document JPL D-79084, 2014, vol. 83.
- [23] N. Steunou, J. D. Desjonquères, N. Picot, P. Sengenès, J. Noubel, and J. C. Poisson, "AltiKa altimeter: Instrument description and in flight performance," *Mar. Geodesy*, vol. 38, pp. 22–42, Oct. 2015.
- [24] E. Peral *et al.*, "The radar-in-a-cubesat (RAINCUBE) and measurement results," in *Proc. IEEE Int. Geosci. Remote Sens. Symp. (IGARSS)*, Valencia, Spain, Jul. 2018, pp. 6297–6300.
- [25] C. Buck, "Cubesat constellation concepts for swath altimetry," in *Proc. IEEE Int. Geosci. Remote Sens. Symp. (IGARSS)*, Yokohama, Japan, Jul. 2019, pp. 8429–8432.
- [26] Y. Li, P. Hoogeboom, P. Lopez-Dekker, and L. Iannini, "AltiCubes: A Ka-band cubesat altimeter constellation concept," in *Proc. ESA 4th Ka-Band Earth Observ. Radar Missions Workshop (KEO)*, Noordwijk, The Netherlands, Nov. 2019, pp. 1–6.
- [27] S.-H. Mok, Y. Choi, H. Bang, and H. Leeghim, "A delayed impulse control strategy for spacecraft formations," *J. Astron. Sci.*, vol. 60, nos. 3–4, pp. 337–365, Dec. 2013.
- [28] C. Boshuizen, J. Mason, P. Klupar, and S. Spanhake, "Results from the planet labs flock constellation," in *Proc. AIAA/USU Conf. Small Satell.*, Aug. 2014.
- [29] G. Filippazzo and S. Dinand, "The potential impact of small satellite radar constellations on traditional space system," in *Proc. 5th Federated Fractionated Satell. Syst. Workshop*, Toulouse, France, Nov. 2017, pp. 1–12.
- [30] Y. Li *et al.*, "AltiCubes: Final report," ESA, Paris, France, Tech. Rep. AO/1-9879/19/NL/FE, 2020, vol. 1.
- [31] M. Martín-Neira, "A passive reflectometry and interferometry system (PARIS): Application to ocean altimetry," *ESA J.*, vol. 17, no. 4, pp. 331–355, 1993.
- [32] X. Capet, J. C. McWilliams, M. J. Molemaker, and A. F. Schepetkin, "Mesoscale to submesoscale transition in the California current system. Part I: Flow structure, eddy flux, and observational tests," *J. Phys. Oceanogr.*, vol. 38, no. 1, pp. 29–43, Jan. 2008.
- [33] T. Moreau *et al.*, "High-performance altimeter Doppler processing for measuring sea level height under varying sea state conditions," *Adv. Space Res.*, vol. 67, no. 6, pp. 1870–1886, Mar. 2021.
- [34] C. Ulivieri *et al.*, "Orbit design analysis for remote sensing satellite constellations," in *Mission Design & Implementation of Satellite Constellations*. Dordrecht, The Netherlands: Springer, 1998, pp. 237–242.
- [35] S.-H. Mok and H. Bang, "Optimal multi-target overflight using ground-track adjustment," *J. Astron. Sci.*, vol. 68, pp. 150–171, Mar. 2021.
- [36] C. Hu, Y. Li, X. Dong, R. Wang, C. Cui, and B. Zhang, "Three-dimensional deformation retrieval in geosynchronous SAR by multiple-aperture interferometry processing: Theory and performance analysis," *IEEE Trans. Geosci. Remote Sens.*, vol. 55, no. 11, pp. 6150–6169, Nov. 2017.
- [37] A. Egido and W. H. F. Smith, "Fully focused SAR altimetry: Theory and applications," *IEEE Trans. Geosci. Remote Sens.*, vol. 55, no. 1, pp. 392–406, Jan. 2017.
- [38] M. I. Skolnik, *Introduction to Radar Systems*. 3rd ed., New York, NY, USA: McGraw-Hill, 2002.
- [39] R. F. Hanssen, *Radar Interferometry: Data Interpretation and Error Analysis*. Dordrecht, The Netherlands: Springer, 2001.
- [40] C. R. McBryde and E. G. Lightsey, "A star tracker design for CubeSats," in *Proc. IEEE Aerosp. Conf.*, Big Sky, MT, USA, Mar. 2012, pp. 1–14.
- [41] J. Dumont *et al.*, *OSTM/Jason-2 Products Handbook*, no. 1. Paris, France: CNES, 2011.
- [42] C. Ubelmann, L.-L. Fu, S. Brown, E. Peral, and D. Esteban-Fernandez, "The effect of atmospheric water vapor content on the performance of future wide-swath ocean altimetry measurement," *J. Atmos. Ocean. Technol.*, vol. 31, no. 6, pp. 1446–1454, Jun. 2014.
- [43] E. Bronner, "SARAL/altiKa products handbook," CNES, Paris, France, Tech. Rep. SALP-MU-M-OP-15984-CN, 2013.
- [44] A. Jäggi *et al.*, "Inter-agency comparison of TanDEM-X baseline solutions," *Adv. Space Res.*, vol. 50, no. 2, pp. 260–271, Jul. 2012.
- [45] L. I. E. A. P. López Dekker and Y. Li, "AltiCubes proposal," ESA, Paris, France, Tech. Rep., AO/1-9879/19/NL/FE, 2019.
- [46] S. Schaer, W. Gurtner, and J. Felten, "IONEX: The ionosphere map exchange format version 1," in *Proc. IGS AC Workshop*, Darmstadt, Germany, 1998, vol. 9, no. 11, pp. 1–12.
- [47] Y. Li, A. M. Guarnieri, C. Hu, and F. Rocca, "Performance and requirements of GEO SAR systems in the presence of radio frequency interferences," *Remote Sens.*, vol. 10, no. 1, p. 82, 2018.
- [48] R. K. Raney, "CryoSat SAR-mode looks revisited," *IEEE Geosci. Remote Sens. Lett.*, vol. 9, no. 3, pp. 393–397, May 2012.
- [49] F. Ulabay and D. Long, *Microwave Radar and Radiometric Remote Sensing*. Norwood, MA, USA: Artech House, 2015.
- [50] E. Peral *et al.*, "Radar technologies for earth remote sensing from cubesat platforms," *Proc. IEEE*, vol. 106, no. 3, pp. 404–418, Mar. 2018.
- [51] S. S. Arnold, R. Nuzzaci, and A. Gordon-Ross, "Energy budgeting for CubeSats with an integrated FPGA," in *Proc. IEEE Aerosp. Conf.*, Big Sky, MT, USA, Mar. 2012, pp. 1–14.
- [52] O. Dogan, F. Uysal, P. Hoogeboom, P. L. Dekker, and Y. Li, "A low SWaP-C radar altimeter transceiver design for small satellites," in *Proc. IEEE Int. IoT. Electron. Mechatronics Conf. (IEMTRONICS)*, Vancouver, BC, Canada, Sep. 2020, pp. 1–5.
- [53] E. Peral *et al.*, "Raincube: The first ever radar measurements from a cubesat in space," *J. Appl. Remote Sens.*, vol. 13, no. 3, 2019, Art. no. 032504.
- [54] M. Weiss, "Synchronisation of bistatic radar systems," in *Proc. IEEE Int. IEEE Int. Geosci. Remote Sens. Symp. (IGARSS)*, Anchorage, AK, USA, Sep. 2004, pp. 1750–1753.
- [55] J. Norton and J. Cloeren, "Precision quartz oscillators and their use aboard satellites," *Fohns Hopkins APL Tech. Dig.*, vol. 15, no. 1, pp. 30–37, 1994.
- [56] G. Nie, F. Wu, K. Zhang, and B. Zhu, "Research on LEO satellites time synchronization with GPS receivers onboard," in *Proc. IEEE Int. Freq. Control Symp. Joint with 21st Eur. Freq. Time Forum*, Geneva, Switzerland, May 2007, pp. 896–900.
- [57] E. Gill, S. D'Amico, and O. Montenbruck, "Autonomous formation flying for the PRISMA mission," *J. Spacecraft Rockets*, vol. 44, no. 3, pp. 671–681, May 2007.
- [58] G. Krieger *et al.*, "TanDEM-X: A satellite formation for high-resolution SAR interferometry," *IEEE Trans. Geosci. Remote Sens.*, vol. 45, no. 11, pp. 3317–3341, Nov. 2007.
- [59] S. D'Amico and O. Montenbruck, "Proximity operations of formation-flying spacecraft using an Eccentricity/Inclination vector separation," *J. Guid., Control, Dyn.*, vol. 29, no. 3, pp. 554–563, May 2006.
- [60] J. L. Junkins and H. Schaub, *Analytical Mechanics of Space Systems*. Reston, VA, USA: American Institute of Aeronautics and Astronautics, 2009.
- [61] R. Kahle, B. Schlepp, and M. Kirschnero, "TerraSAR-X/TanDEM-X formation control—first results from commissioning and routine operations," *J. Aerosp. Eng., Sci. Appl.*, vol. 3, no. 2, pp. 16–27, May 2011.
- [62] A. W. Koenig and S. D'Amico, "Robust and safe N-spacecraft swarming in perturbed near-circular orbits," *J. Guid., Control, Dyn.*, vol. 41, no. 8, pp. 1643–1662, Aug. 2018.
- [63] K. Matsuka, D. Scharf, N. Filipe, C. Seubert, and D. Bayard, "Relative sensing, control precision, and mission Delta-V trade-offs for precision formation flying in planetary orbit," *J. Guid., Control, Dyn.*, vol. 42, no. 5, pp. 992–1006, May 2019.
- [64] N. Chahat, R. E. Hodges, J. Sauder, M. Thomson, E. Peral, and Y. Rahmat-Samii, "CubeSat deployable Ka-band mesh reflector antenna development for earth science missions," *IEEE Trans. Antennas Propag.*, vol. 64, no. 6, pp. 2083–2093, Jun. 2016.

- [65] R. E. Hodges, N. Chahat, D. J. Hoppe, and J. D. Vacchione, "A deployable high-gain antenna bound for MARS: Developing a new folded-panel reflectarray for the first CubeSat mission to Mars," *IEEE Antennas Propag. Mag.*, vol. 59, no. 2, pp. 39–49, Apr. 2017.
- [66] B. Lim *et al.*, "Development of the radiometer atmospheric cubesat experiment payload," in *Proc. IEEE Int. Geosci. Remote Sens. Symposium (IGARSS)*, Melbourne, VIC, Australia, Jul. 2013, pp. 849–851.



Yuanhao Li (Member, IEEE) received the B.S. degree in information engineering and the Ph.D. degree in information and communication engineering from Beijing Institute of Technology (BIT), Beijing, China, in 2012 and 2018, respectively.

From 2016 to 2017, he has worked as a Visiting Researcher with the Dipartimento di Elettronica e Informazione, Politecnico di Milano (PoliMi), Milan, Italy. In 2018, he was the Research Scientist of the Radar Research Laboratory, BIT. From October 2018 to January 2021, he was a Post-Doctoral Researcher with the Department of Geoscience and Remote Sensing, Delft University of Technology (TU Delft), Delft, The Netherlands. He is currently an Associate Professor with the School of Information and Electronics, BIT. His research interests include radar system design and signal processing, interferometric synthetic aperture radar (InSAR)/differential InSAR (D-InSAR) technique, and radar altimeters constellations.

Dr. Li was a recipient of the Chinese Institute of Electronics Youth Conference Excellent Paper Award in 2014.



Peter Hoogeboom received the M.S.E. degree in electrical engineering from Delft University of Technology (TU Delft), Delft, The Netherlands, in 1975.

He is currently a Professor of radar and earth observation with the Department of Geoscience and Remote Sensing, TU Delft. He has been involved in airborne and spaceborne radar instrument studies, calibration, and applications. After his retirement in 2017, he continued his part-time work at TU Delft, focusing on miniaturized radar (altimeter) instruments for applications with small satellites and CubeSats.



Paco López Dekker (Senior Member, IEEE) was born in Nijmegen, The Netherlands, in 1972. He received the Ingeniero degree in telecommunication engineering from the Universitat Politècnica de Catalunya (UPC), Barcelona, Spain, in 1997, the M.S. degree in electrical and computer engineering from the University of California at Irvine, Irvine, CA, USA, in 1998, under the Balsells Fellowship, and the Ph.D. degree from the University of Massachusetts at Amherst, Amherst, MA, USA, in 2003, with a focus on clear-air imaging radar systems to study the atmospheric boundary layer.

From 1999 to 2003, he was with the Microwave Remote Sensing Laboratory, University of Massachusetts at Amherst. In 2003, he was with Starlab, Barcelona, where he was involved in the development of global navigation satellite system (GNSS)-R sensors. From 2004 to 2006, he was a Visiting Professor with the Department of Telecommunications and Systems Engineering, Universitat Autònoma de Barcelona, Barcelona. In 2006, he joined the Remote Sensing Laboratory, UPC, where he conducted the research on bistatic synthetic aperture radar (SAR) under a five-year Ramon y Cajal Grant. From 2009 to 2016, he led the SAR Missions Group, Microwaves and Radar Institute, German Aerospace Center, Weßling, Germany. The focus of the SAR Missions Group was the study of future SAR missions, including the development of novel mission concepts and detailed mission performance analyses. Since 2016, he has been an Associate Professor with the Faculty of Civil Engineering and Geosciences, Delft University of Technology, Delft, The Netherlands. He is currently a Principal Investigator for the Harmony Earth Explorer 10 mission candidate. His research interests include (In)SAR time series analysis, the use of SAR to study ocean processes, and the development of distributed multistatic radar concepts.



Sung-Hoon Mok was born in South Korea, in 1986. He received the Ph.D. degree from Korea Advanced Institute of Science and Technology (KAIST), Daejeon, South Korea, in 2014.

He has worked as a Post-Doctoral Researcher with Delft University of Technology (TU Delft), Delft, The Netherlands, from 2019 to 2020. He is currently a Senior Researcher with the Defense and Space Center, Agency for Defense (ADD) Development, South Korea. He has (co)authored more than 35 journal articles and conference papers. His research interests include distributed space systems, relative orbit guidance and control, attitude determination and control, and mission planning.



Jian Guo received the B.Sc. and M.Sc. degrees in engineering from Northwestern Polytechnical University, Xi'an, China, in 1998 and 2001, respectively, and the Ph.D. degree in mechanical engineering from the University of Leeds, Leeds, U.K., in 2010.

He is currently an Associate Professor with the Department of Space Engineering, Delft University of Technology (TU Delft), Delft, The Netherlands. He is also the Theme Leader of the TU Delft Space Institute. His research interests include small satellites, spacecraft guidance navigation and control, distributed space systems, and space robots.

Christopher Buck was born in Cambridge, U.K., in 1961. He received the B.S. degree in electronic and electrical engineering from the University of Surrey, Guildford, U.K., in 1984, and the M.Sc. degree in geographical information systems from Vrije Universiteit, Amsterdam, The Netherlands, in 2002.

Since 1994, he has been with the Radio Frequency Payload Systems Division, European Space Research and Technology Centre, European Space Agency (ESA), Noordwijk, The Netherlands, working in the area of microwave remote sensing. Originally on the ERS-2 Active Microwave Instrument-Synthetic Aperture Radar (AMI-SAR) and later ENVISAT Advanced Synthetic Aperture Radar (ASAR), he has also been responsible for various microwave remote sensing activities in the areas of synthetic aperture radar (SAR) calibration, ice sounding, and interferometry. Most recently, his research activities have been mainly directed toward global navigation satellite system (GNSS)-R, atmospheric radar, and ocean surface current mapping by orthogonal-beam along-track interferometric SAR (InSAR).

Mr. Buck is the Co-Chair of the Global Navigation Satellite Systems Working Group of the Instrumentation and Future Technologies Technical Committee of the IEEE Geoscience and Remote Sensing Society.